Astronomy & Astrophysics manuscript no. noInter_final
May 22, 2014
©ESO 2014

arXiv:1405.5222v1 [astro-ph.GA] 20 May 2014

Kinematic alignment of non-interacting CALIFA galaxies

Quantifying the impact of bars on stellar and ionised gas velocity field orientations

J. K. Barrera-Ballesteros[1,2,⋆], J. Falcón-Barroso[1,2], B. García-Lorenzo[1,2], G. van de Ven[3], J. A. L. Aguerri[1,2], J. Mendez-Abreu[1,2,4], K. Spekkens[5], S. F. Sánchez[6,7,8], B. Husemann[9,10], D. Mast[6,8], R. García-Benito[6], J. Iglesias-Paramo[6,8], A. del Olmo[6], I. Márquez[6], J. Masegosa[6], C. Kehrig[6], R. A. Marino[11], L. Verdes-Montenegro[6], B. Ziegler[12], D. H. MacIntosh[13], J. Bland-Hawthorn[14], C. J. Walcher[10], and the CALIFA Collaboration

(Affiliations can be found after the references)

May 22, 2014

ABSTRACT

We present 80 stellar and ionised gas velocity maps from the Calar Alto Legacy Integral Field Area (CALIFA) survey in order to characterize the kinematic orientation of non-interacting galaxies. The study of galaxies in isolation is a key step towards understanding how fast-external processes, such as major mergers, affect kinematic properties in galaxies. We derived the global and individual (projected approaching and receding sides) kinematic position angles (PAs) for both the stellar and ionised gas line-of-sight velocity distributions. When compared to the photometric PA, we find that morpho-kinematic differences are smaller than 22 degrees in 90 % of the sample for both components; internal kinematic misalignments are generally smaller than 16 degrees. We find a tight relation between the global stellar and ionised gas kinematic PA consistent with circular-flow pattern motions in both components. This relation also holds generally in barred galaxies across the bar and galaxy disk scales. Our findings suggest that even in the presence of strong bars, both the stellar and the gaseous components tend to follow the gravitational potential of the disk. As a result, kinematic orientation can be used to assess the degree of external distortions in interacting galaxies.

Key words. Galaxies: kinematics and dynamics – Galaxies: photometry – Galaxies: structure – Galaxies: evolution

1. Introduction

To first order, galaxies are rotationally-supported disk systems (for a historical review see e.g., Sofue & Rubin 2001). The observed line-of-sight velocity distributions are expected to show a regular rotation pattern in the form of the so-called "spider diagram", with the position angle (PA) of the minimum and maximum aligned with the optical major axis. However, several physical processes can disturb this regular behaviour. On the one hand, kinematic perturbations can be induced by external factors such as ram-pressure stripping (e.g., Kronberger et al. 2008) or galactic mergers (e.g., Naab & Burkert 2003). On the other hand, kinematic departures from regular rotation can be due to internal instabilities such as spiral arms or bars (Binney & Tremaine 2008; Sellwood 2013). To disentangle the perturbations due to external processes it is necessary first to study in detail the possible kinematic perturbations due to internal processes in both stars and gas.

Integral-field spectroscopy (IFS) is a unique tool to study the kinematic properties across the entire galaxies. Even though 3D spectroscopic surveys are now feasible for a large set of galaxies (e.g.: GHASP, GHαFaS, ATLAS^{3D}, SAMI; Epinat et al. 2008; Hernandez et al. 2008; Cappellari et al. 2011; Croom et al. 2012), these surveys have usually focused on the study of the kinematics of early-type systems (e.g.: SAURON, ATLAS^{3D}; Emsellem et al. 2004; Krajnović et al. 2011) or on specific wavelength range like Hα range in spiral galaxies in different environments (e.g., GHASP, and GHαFaS Fathi et al. 2009; Epinat et al. 2008).

The CALIFA survey (Sánchez et al. 2012) provides an unique opportunity to study simultaneously the stellar and ionised gas global kinematics in a sample of galaxies that covers a wide range of morphological types, stellar masses and environments. The spectral and spatial coverage provided by the CALIFA IFS data allow us to study the effect of structures such as bars in non-interacting galaxies on the global kinematics. Bars are frequent elliptical-like structures present in disk galaxies. About 40−50 % of nearby disk galaxies observed in optical wavelengths show bars features (e.g., Marinova et al. 2007; Barazza et al. 2008; Aguerri et al. 2009). This fraction is even higher (about 60−70 %) for near-infrared observations (e.g., Eskridge et al. 2000; Knapen et al. 2000; Menéndez-Delmestre et al. 2007). Hydrodynamical simulations of these systems show that the bar component contributes only between 10 and 20 % of the disk potential (e.g., Scannapieco et al. 2010), and yet it can produce important changes in the gas dynamics. Bars are thought to be very efficient in redistributing angular momentum, energy and mass in both luminous and dark matter components (e.g., Weinberg 1985; Debattista & Sellwood 1998, 2000; Athanassoula 2003; Martinez-Valpuesta et al. 2006; Sellwood 2006; Sellwood & Debattista 2006; Villa-Vargas et al. 2009). The effects of this angular momentum redistribution is different in gas and stars due to their different properties (e.g., Thielheim & Wolff 1982). For example, flows are observed within the co-

⋆ e-mail: jkbb@iac.es

rotation radius towards the galaxy centre only in the gas component (e.g., Rozas et al. 2002).

The aim of this paper is to characterize the stellar and the ionised gas kinematics for a sample of non-interacting galaxies by means of their global orientation. In a companion paper (Barrera-Ballesteros et al., in preparation) we will use the results of the present study to quantify how much the kinematic of a sample of interacting galaxies differentiates with respect to the kinematics of isolated ones. In other words, the result from this work will yield a yardstick describing kinematic distortions due to internal processes with which to compare to kinematic disturbances induced by major merger events.

The paper is organized as follows. In Section 2, we present the sample as well as the methods for extracting the stellar and ionised gas kinematics. The procedure used to derive directly the kinematic PA from the velocity maps is presented in Section 3. Section 4 presents the kinematic characterization of the non-interacting galaxies: morpho-kinematic and kinematic misalignments are compared against different bar strengths as well as at different radii of barred galaxies. The impact of bars in the velocity field is discussed in Section 5. Our findings and main conclusions are summarized in Section 6.

2. Sample and observations

2.1. Sample selection

The sample presented in this work is drawn from the CALIFA mother sample (Sánchez et al. 2012) observed until November 2013. This mother sample includes 939 galaxies, selected from the SDSS DR7 (Abazajian et al. 2009). The selection criteria is such that galaxies included are in the nearby Universe with redshifts $0.005 < z < 0.03$ and their isophotal diameter in the SDSS r-band is $45'' \lesssim D_{25} \lesssim 80''$.

Using the SDSS r-band images of the observed galaxies we select 80 galaxies without evident signatures of interaction such as tidal tails, bridges, rings, shells or any other morphological distortion caused by a merging. Moreover, we consider galaxies isolated from companions within a physical radius of 250 kpc, a systemic velocity difference smaller than 1000 km s^{-1} and a difference in magnitude in the SDSS r-band images larger than 2 mag (position and systemic velocities were taken from NED[1]). We use a conservative physical radius for rejecting close companions with respect to pairs-survey criteria (e.g., Ellison et al. 2008). The systemic velocity selection criteria is supported by recent cosmological simulations (Moreno et al. 2013). Finally, we also selected those galaxies for which stellar and ionised gas signal-to-noise (S/N) ratios allow us a reliable estimation of their kinematic properties (see section 2.2).

It is important to note that these selection criteria does not exclude from our sample galaxies with minor companions or galaxies located in the outskirts of groups. However, we estimate the perturbation caused by tidal forces induced by companions by means of the f-value (Varela et al. 2004). Values larger than -2 are required to produce sizeable effects on a disk galaxy. We were able to measure in 71 objects the f-value. We found that 95% of these galaxies have f-values smaller than -2 with a mean value of -4.0. This suggests that our sample is a fairly representation of isolated galaxies. In fact, 10 galaxies from our sample are also part of the AMIGA sample (Analysis of the interstellar Medium of Isolated GAlaxies, Verdes-Montenegro et al. 2005, CALIFA id: 2, 30, 131, 152, 275, 743, 748, 777, 779, 856). AMIGA sample is defined based on strict isolation criteria, and shows different physical properties at all wavelengths studied so far than galaxies in denser environments (even field galaxies). These 10 galaxies are located in the region of lower tidal forces and number density of AMIGA full sample (Fig. 6 in Verley et al. (2007)).

Our non-interacting sample includes different morphological types, bar strengths and a relatively wide range of luminosities ($-24 \lesssim M_r \lesssim -19$; where M_r is the absolute magnitude in SDSS r-band). Morphological types and bar strengths were obtained by visual inspection of the SDSS r-band images by different members of the collaboration (Walcher et al., in preparation, see also table B.1). Even more, the sample is dominated by Sbs and Sc morphological types, which are also the dominant population of the AMIGA sample, hence characteristic of isolated galaxies. Finally, from a visual inspection of the velocity maps we exclude from our sample the early-type galaxy NGC 5623. This galaxy presents a stellar counter-rotating disk, presumably originated from an early encounter, and thus it will be included in the sample of interacting galaxies of Barrera-Ballesteros et al. (in prep.).

2.2. CALIFA velocity maps

Observations were carried out using the PPAK instrument at Calar Alto Observatory (Roth et al. 2005). Its main component consists of 331 fibers of 2.″7 diameter each, concentrated in a single hexagon bundle covering a field-of-view of $74'' \times 64''$, with a filling factor of $\sim 60\%$. Three dithered pointings are taken for each object to reach a filling factor of 100% across the entire FoV. The final data cube consists of more than 4000 spectra at a sampling of $1'' \times 1''$ per spaxel (see details in Husemann et al. 2013). The CALIFA survey has two spectral setups, V500 and V1200, low and intermediate resolution, respectively. Objects included in this work have been observed in the V500 setup. This setup has a nominal resolution of $\lambda/\Delta\lambda \sim 850$ at $\sim$5000Å and its nominal wavelength range is 3745−7300Å.However, the final data cube has an homogenized spectral resolution (FWHM) over the entire wavelength range of 6.0Å and the wavelength sampling per spaxel is 2.0Å. The total exposure time per pointing is fixed for all the observed objects to 45 min. The data reduction is performed by a pipeline designed specifically for the CALIFA survey. Detailed reduction process is explained by Sánchez et al. (2012) and improvements on this pipeline are presented by Husemann et al. (2013).

The stellar kinematic extraction method for the CALIFA survey will be presented in Falcón-Barroso et al. (in prep.). Here we highlight the main steps. Spaxels with continuum S/N < 3 in the original V500 cube were considered unreliable and therefore not considered in further analysis. To achieve a minimum S/N of 20, we used a Voronoi-binning scheme for optical IFS data implemented by Cappellari & Copin (2003). We will refer to these Voronoi bins as "voxels". From this selection in the continuum S/N, a large fraction of the voxels (~80%) have the same size as the spaxels of the cube. The remaining fraction of the voxels are located in the outer regions of the galaxies and include a range between three or five spaxels. To derive the line-of-sight velocity maps, for each cube, a non-linear combination of a subset of stellar templates from the Indo-U.S. library (Valdes et al. 2004) is fit to each voxel using the penalized pixel-fitting method (pPXF, Cappellari & Emsellem 2004). Errors for each voxel, determined via Monte Carlo simulations, range from 5 to 20 km s^{-1} for inner to outer voxels, respectively. Note that these uncertain-

[1] NASA/IPAC Extragalactic database. http://ned.ipac.caltech.edu/

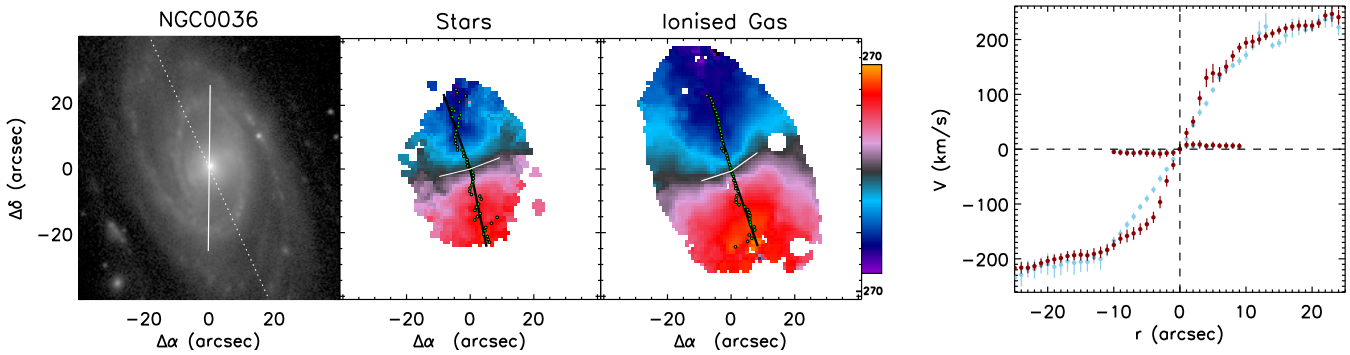

Fig. 1. Example of the method used to determine projected kinematic position angles (PAs) from the velocity maps of the galaxy NGC 36. Left most panel shows the SDSS *r*-band image of the galaxy. White solid line represents the photometric PA measured at the same galactocentric distance as the kinematic PA (PA_{morph}, measured from the *r*-band image; see section 3). Dashed line represents the photometric PA measured at the outermost isophotes of the image (PA^{out}_{morph}, see section 4.3). Middle-left and middle-right panels show the stellar and ionised gas velocity maps, respectively. Green points highlight the locations where the maximum velocity is located at given radius, determined from the position-velocity diagram. Black lines for each kinematic side represent the average kinematic PA (PA_{kin}), while black thin lines along the zero-velocity curve show the average minor kinematic PA. Right panel shows the distance from the galactic centre versus the maximum for the stellar (blue points) and ionised gas (red points) components. The curve along 0 km s^{-1} represent the velocities along the zero-velocity curve. The error bars represent the uncertainty in velocity determined from Monte Carlo simulations.

ties are smaller than the spectral sampling per spaxels from the data cubes. Since each spaxel offers a wide range of absorption lines to fit its line-of-sight velocity, the spectral location of these absorption features can be determine even at scales smaller than the spectral sampling. Figure 1 (middle-left panel) shows an example of a stellar kinematic maps for one of our galaxies

The detailed description of the ionised-gas kinematic extraction method for the CALIFA survey is provided by García-Lorenzo et al. (2014, submitted). Briefly, to obtain the ionised-gas emission in each spaxel we subtracted the stellar continuum spectra derived from the best stellar pPXF fit in its corresponding voxel. No binning was done for the ionized gas. We assumed that the stellar populations in each voxel are rather smooth and do not change from spaxel to spaxel within each voxel. A cross-correlation (CC) method is used to measure the velocity of the ionised-gas (see García-Lorenzo 2013, for details on the method). The method compares the spectrum in each spaxel in a given wavelength range with a template that includes the Hα+[NII]$\lambda\lambda$6548,6584 emission lines (6508−6623Å). The template corresponds to a Gaussian model for each emission line in the given wavelength range, shifted to the systemic velocity reported in NED and assuming a velocity dispersion equals to the instrumental resolution ($\sigma \sim 90$ km s^{-1} at the Hα emission line). We selected spaxels with S/N $>$ 8 in this emission line for the ionised gas velocity maps. García-Lorenzo et al. (2014, submitted) present examples on the kinematic fitting per spaxel and the extraction of the ionized gas component. Fig. 1 (middle-right panel) shows an example of an ionised-gas velocity maps. Estimated uncertainties in the location of the maximum of the CC function are ∼10 km s^{-1}. Both the pPXF and the CC methods are able to determine velocity dispersion maps however, due to the low spectra resolution of the V500 data we did not attempt any further analysis of these maps. They are also not required for the work presented here.

3. Kinematic position angles from velocity maps

Appendix C shows the complete set of stellar and ionised gas velocity maps for the galaxies in this study. Some of them are also presented in Falcón-Barroso et al. (in prep., for stellar kinematics in the V1200 setup) and García-Lorenzo et al. (2014, submitted for the ionised gas).

In the last years, several analytic methods have been developed to determine kinematic properties from two-dimensional velocity distributions. These models consider symmetric velocity distributions, either by assuming a thin disk geometry (e.g., Barnes & Sellwood 2003; Epinat et al. 2008), pure-circular motion on elliptical galaxies (Krajnović et al. 2006) or symmetrical radial distortions with respect to some axis (Spekkens & Sellwood 2007). Even though these methods yield good results for symmetric velocity maps, they may provide (depending on its use) biased or uncertain results for galaxies with strong departures from order motions.

The aim of this paper is to establish the observed (i.e., projected) typical ranges of kinematic parameters expected for non-interacting galaxies. From those kinematic values, we will be able to shade some light on the possible kinematic distortions induced by an interaction. For this reason, we provide in this study a quantitative characterization of the kinematics of galaxies through parameters derived *directly* from their stellar and ionised gas velocity distributions. No assumption on the behaviour of the galactic components is made. We will use the same method on our sample of interacting galaxies in order to make a consistent comparison. A pure-rotational velocity field can be caracterized by several parameters: kinematic centre, systemic velocity, global orientation of the field (i.e., kinematic PA), and its inclination with respect to the sky's plane. In this study we restrict ourselves only to kinematic projected properties of the sample. We consider that an estimation of the inclination via the velocity distribution would require assuming an intrinsic behavior on the kinematic component (e.g., tilted-ring modeling, Józsa et al. 2007). Although, this could be the case of some of the non-interacting galaxies presented in this study (restricted even only to the nebular component), it might not be the case for highly asymmetric velocity fields, such as those exhibit by interacting/merging galaxies. In the work presented here we focus mainly on the characterzation of the velocity fields via their different components kinematic PAs.

In order to determine the global orientation of the velocity maps first it is necessary to set the kinematic centre. For an ideal pure rotating disk the kinematic centre should be at the position

with the largest velocity gradient (or gradient peak, GP hereafter) and in agreement with optical nucleus. The reader is refered to García-Lorenzo et al. (2014, submitted) for details of the method used to determine the velocity gradient in the CALIFA ionized gas velocity fields. Briefly, in a region of $10'' \times 10''$ centred in the optical nuclei we determine the velocity gradient in each spaxel with respect to the surrounding spaxels. Then, we select the positions where the velocity gradient is larger than its average inside this box. Finally, the GP is estimated from the weighted average location of the selected positions, using as weights the velocity gradient at each location.

For an observed velocity field the GP does not always coincided with the optical nucleus (ON hereafter). Taking the size of the original fiber as the minimum distance to report an offset between the GP and ON (i.e., 2.7″). We find that a large fraction of the sample in their stellar component do not present a significant offset between these two positions (69/80) with a mean offset of 1.5 and standard deviation of 1.1 arcsecs. In the rest of the stellar velocity fields this offset is due to possible SNe in the central region (e.g., NGC 7478) or the possibility in barred galaxies that the GP is located at the end of bar (e.g. NGC 6004). The ionized gas present similar offsets (mean offset of 1.3 and standard deviation of 0.9 arcsecs). However the fraction of galaxies with small offsets is larger (74/80). The galaxies with large offsets are either edge on galaxies (e.g., UGC 841) or patchy in emission (e.g., NGC 4956). Finally, as kinematic centre we choose either ON or GP, depending on the best symmetry of the rotational curve (see details below). In all the cases with large offset in the GP (in both components) the ON yields a more symmetric velocity curve than the GP. This yield that in 21/80 and 5/80 velocity fields the ON was selected as the kinematic centre for the stellar and ionized gas components, respectively. As we note above most of the offsets are smaller than the original spatial resolution of the instrument, in particular, for the stellar component where spatial binning is done (although small for the nuclear region) this yield a larger number of fields where the ON was selected as kinematic centre. In tables B.2 and B.3 we list the gradient peak location with respect to the optical centre when the choice for the kinematic centre was the GP, and the systemic velocity derived for both components as the mean value within a 2.7″ radius of the kinematic centre.

The major (projected) kinematic axis (PA_{kin}, hereafter) provides a measurement of the global kinematic orientation. It can be determined directly from the positions of the spaxels defining the kinematic lines of nodes (Nicholson et al. 1992). In practice, we plot the radial velocity for all the spaxels up to a given radius in a position-velocity diagram centred in the kinematic centre previously assigned (see right panel of Fig. 1). We then choose those spaxels with the maximum (minimum) projected velocity at the receding (approaching) side at different radii. Finally, for each side, we identify the selected spaxels in the velocity map. The average of their polar coordinates provides an estimation of PA_{kin} and their standard deviation (δPA_{kin}) measures the scatter of these points around the straight line defining the kinematic PA. Following a similar procedure, we also determine the minor (receding and approaching) kinematic PA by selecting the spaxels with the lowest velocity differences respect to the kinematic center. To compare the stellar and the ionised gas kinematic PA we pick the common maximum radius where both components can be measured. Although PA_{kin} is usually defined as the angle between the north and the receding side of the velocity field (e.g., Schoenmakers et al. 1997), for the sake of homogeneity, we report the approaching and receding kinematic PAs independently ($PA_{kin,app}$ and $PA_{kin,rec}$) between 0 and 180 degrees from

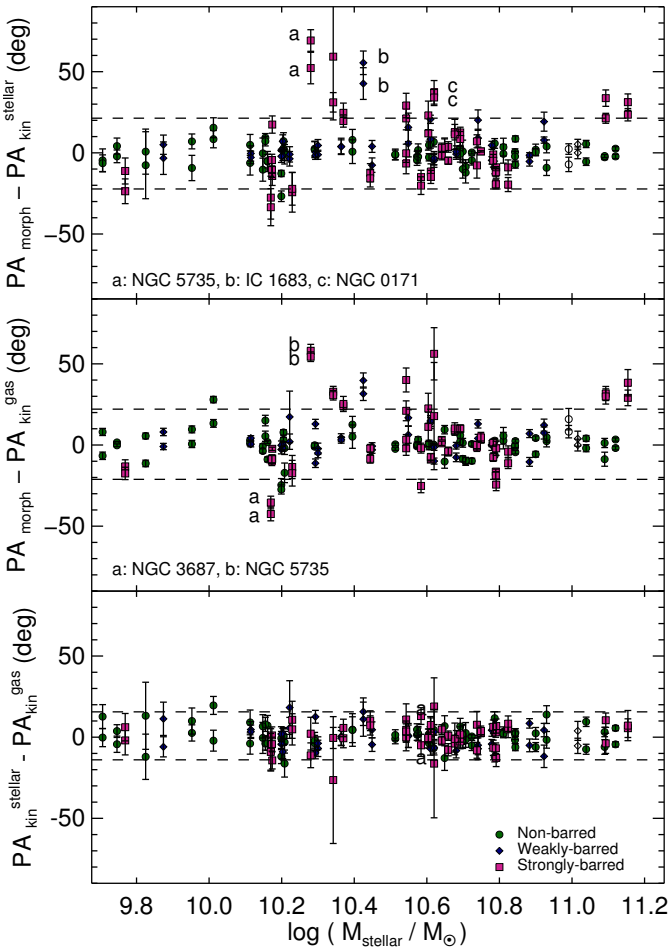
PA morph – PA kin stellar (deg)
PA morph – PA kin gas (deg)
PA kin stellar - PA kin gas (deg)
a: NGC 5735, b: IC 1683, c: NGC 0171
a: NGC 3687, b: NGC 5735
Non-barred
Weakly-barred
Strongly-barred
log (M stellar / M⊙)

Fig. 2. Difference between the morphological PA (PA_{morph}) and kinematic PA (PA_{kin}) against the total stellar mass for the stellar (top) and the ionised gas (middle), as well as the stellar versus ionised-gas kinematic PA (bottom). Both kinematic sides of the velocity maps were compared with PA_{morph} (top panels) and between each component (bottom panel). In each panel, the green-filled circles represent the non-barred galaxies, blue diamonds are weakly-barred galaxies and violet squares correspond to barred galaxies. For early-type galaxies we use open circles. Dashed lines represent the 2σ dispersion of the sample. Labels indicate the 3σ outliers. Error bars are determined from Monte Carlo simulations.

North to East. Typical errors in PA_{kin} and δPA_{kin} are of the order of 7 ° obtained from Monte Carlo simulations. We have also investigated the uncertainties introduced by the Voronoi binning in the stellar velocity maps (by artificially increasing the level of binning in a few of our galaxies) and established that they could bias the determination of PA_{kin} at most 4°.

In this study, for comparison, we also estimate the photometric orientations PA_{morph} of the galaxies by fitting an ellipse model using the standard task *ellipse* of IRAF[2] on the isophotes of the SDSS *r*-band image at two galactocentric distances: 1) at the same galactocentric distance where PA_{kin} are derived (PA_{morph}, see solid white line in left panel of Fig. 1) and 2) at the outer most isophotes of the image (PA^{out}_{morph}, see dotted white line in

[2] IRAF is distributed by the Optical Astronomy Observatory, which is operated by the Association of Universities for research in Astronomy (AURA) under cooperative agreement with the National Science Fundation

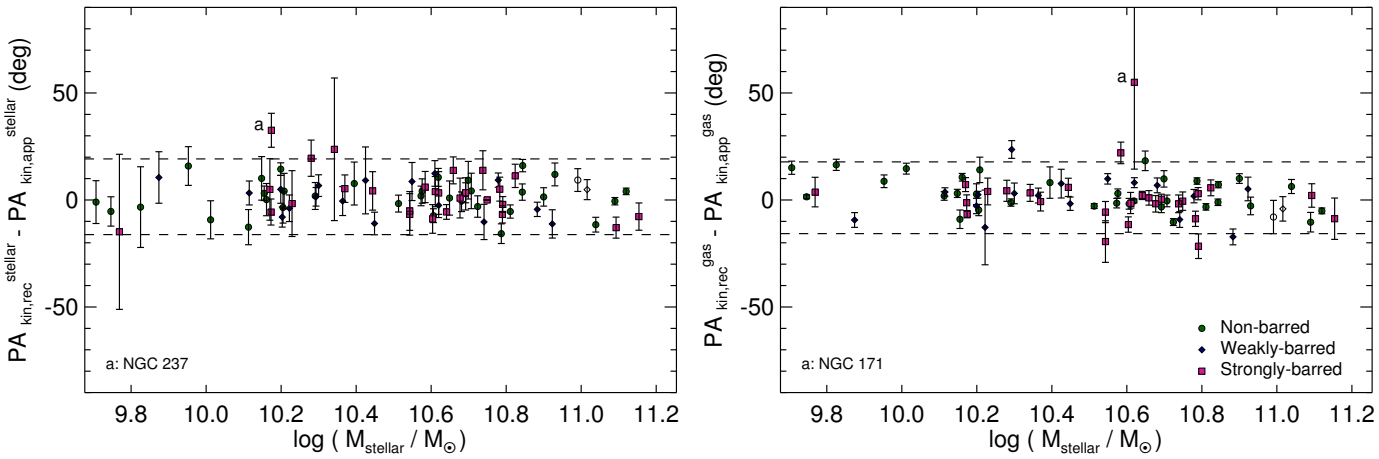

Fig. 3. Internal kinematic misalignment between the receding PA ($PA_{kin,rec}$) and approaching ($PA_{kin,app}$) kinematic position angle against the stellar mass. In each panel the green-filled circles represent the non-barred galaxies, blue diamonds correspond to weakly-barred galaxies and violet squares represent the barred galaxies. Open circles represent the early-type galaxies. Dashed lines represent the 2σ dispersion of the sample ($\sim$15°). Labels indicate the 3σ outliers. Error bars at the left-top of each panel represent the typical error determined from Monte Carlo simulations.

left panel of Fig. 1). We use the ellipticity of the latter (ϵ) as an homogeneous proxy for the inclination of the galaxies in our sample (see Table B.1). All the position angles used in this work, as well as the radial distances where they have been computed, are presented in Tables B.2 and B.3.

4. Kinematic alignment of galaxies

4.1. Global morpho-kinematic misalignments

In Fig. 2 we show the morpho-kinematic PA misalignment (i.e., $PA_{morph} - PA_{kin}$) for the stellar and ionised-gas components (top and middle panels, respectively) against the total stellar mass of the galaxies (from Walcher et al., in preparation). Since there is no preference between the kinematic approaching and receding PA, both of them were compared with respect to PA_{morph}. We do not find any trend between the stellar mass and the morpho-kinematic PA misalignment, in any component, for our sample of galaxies.

About 90% of the galaxies have morpho-kinematic misalignments smaller than 21(stellar)/ 22 (ionised gas) degrees. The mean misalignment and standard deviation are $\sim$0° and $\sim$10°, respectively in both components. This indicates a global agreement between morphology and kinematics regardless the morphological type or bar strength. Barred galaxies present in both components the larger morpho-kinematic difference and the larger error bars (see tags in Fig. 2). On the one hand, larger differences in the stellar component are observed in IC 1683, NGC 5735, and NGC 171. For the two former galaxies the kinematic PA is similar to PA^{out}_{morph} rather than PA_{morph}. However PA_{kin} of NGC 171 is not similar to any of the photometric PA presented here (see Fig. 4). On the other hand for the ionised component, NGC 3687 and NGC 5735 present dissagrements with the photometric and kinematic PA. Similarly as in the stellar component, this galaxies seems to be more aligned to PA^{out}_{morph} than PA_{morph}. In Sec. 4.3, we study the impact of deriving the kinematic PA at different radius, in particular for barred galaxies.

Krajnović et al. (2011) found that for 90% of the ATLAS^{3D} galaxies displayed stellar morpho-kinematic misalignments smaller than 16° in their stellar component. From a sample of 24 early-type bulges, Falcón-Barroso et al. (2006) found that 80% showed stellar morpho-kinematic differences smaller than 20°. Our results, based on a sample of non-interacting galaxies with a wide range of morphological types, are consistent with those findings. For the ionised-gas, the Fabry-Perot survey of late-type spirals and irregular galaxies, GHASP (Epinat et al. 2008), reported a 85% of the objects with morpho-kinematic misalignments smaller than 15°. These results are also in agreement with our findings. Similar results have also been found for smaller samples (e.g. Kutdemir et al. 2008).

Although we present along this study projected kinematic properties of non-interacting galaxies, in Appendix A we study the possible impact of the inclination for the determination of kinematic properties. In Fig. A.2 we plot the previous morpho-kinematic misalignments with respect to the photometric ellipticity as a proxy for the inclination (ϵ, see Sec. 3). As is expected, larger misalignments are found at low ellipticities whereas at high ellipticities the morpho-kinematic misalignements get reduced due to the projection effects. However, we suggest that even at low ellipticities this misalignments reduced significantly (see Sec. 4.3).

Our results suggest that for a non-interacting galaxy the misalignment between the photometric and global (stellar- and/or ionised gas-) kinematic orientation is small for a wide range of morphologies and stellar masses (smaller than 20°, with a mean value of $\sim$ 0°). This also held for galaxies with strict isolation critera (i.e., AMIGA subsample), where the average misalignment for these galaxies is $\sim$1° with a standard deviation of 8° and 5° for the stellar and ionized gas component, respectively. As we noted previously only a small fraction of galaxies (2/80, barred) show large morpho-kinematic misalignments.

In the bottom panel of Fig. 2 we show the difference between the stellar and ionised gas kinematic PA (i.e.$PA^{stellar}_{kin} - PA^{gas}_{kin}$). As in previous plots, we separate our sample according to their different bar strengths. In this stellar mass range, we do not find any trend. Barred and non-barred galaxies present similar alignments between their components. In fact, the mean difference for these components orientations is $\sim$1° with a standard deviation of $\sim$7°. For 90% of the galaxies, the global orientation of the stellar and the ionised gas velocity fields agrees, with differences smaller than 16°. The only galaxy that seems to present

large kinematic misalignment between both components is the late-type barred galaxy NGC 171. The large uncertainties in the ionized gas component as well the fact that the locations of maximum velocity present a large deviation from a straight line in the gas component suggest that the strong bar is the driver that distorted the ionised gas velocity field. From the SDSS *r*-band image, this object presents a bar as large as the FoV of the instrument with an extended ring. This is the only galaxy with these features in the sample presented here. In Fig. A.4 we plot these misalignments respect to the ellipticity. For a wide range of inclinations the alignment between both components is consistent. Summarizing, our measurements reveal small morpho-kinematics misalignments for both component as well as small stellar versus gas kinematic misalignments for barred galaxies, comparable to those for non-barred galaxies. At the spatial and spectral resolution of CALIFA survey, both components thus seem to follow a similar kinematic pattern even in the presence of bars.

4.2. Internal kinematic PA misalignments

In Sec. 3 we estimated kinematic PA from the approaching and receding side as well as their departures from a straight line ($PA_{kin,rec}$, $PA_{kin,app}$, $\delta PA_{kin,rec}$, $\delta PA_{kin,app}$). This allows us to study the internal kinematic misalignment, defined as $|PA_{kin,rec} - PA_{kin,app}| - 180°$, which should be zero for a regular rotational pattern. Figure 3 presents these misalignments for the stellar (left) and the ionised gas (right) components.

We find that $\sim 92\%$ of the objects have internal kinematic misalignment smaller than 15° for both the stellar and the ionised gas. This is for different stellar masses and ellipticities (see Fig. A.3). Assuming that our objects are a representative sample of isolated galaxies, we suggest that any distortion in the line-of-sight velocity distribution that produces a kinematic misalignment larger than those values is not caused by internal processes. The kinematic deviations from a straight line δPA_{kin} range from 5° to 40° in both components for a large fraction of the sample ($\sim 90\%$). The mean value of these deviations is twice for the stellar component with respect to the ionized gas ($\sim 15°$ and $\sim 7°$). Their standard deviation is also twice for stars respect to the stellar component ($\sim 8°$ and 4°, respectively). In Fig. 5(top-panel) we plot the distribution of δPA_{kin} for different barred strengths. The fact that the mean deviation of the stellar component is almost twice the deviation from the ionized gas could be explained by different factors. On the one hand, although we are allow to determine in each spaxel the stellar velocity with relatively small uncertainty, the change of velocity for joint spaxels could be smaller than the spectral resolution leading in a higher scatter in the positions of maximum velocity. On the other hand, the method used here to derived kinematic properties is entirely based on the symmetry that a pure rotational velocity field should display. Therefore, any deviation translates in a perturbation in any of the parameters we are using to quantify or velocity fields. Small δPA_{kin} in the ionized gas indicates that gas lies in a thin disk, while the stellar component present 'dynamical-heated' structures (e.g., dynamical heated disk, pressure-supported bulge, etc).

As we mention above, the barred galaxy NGC 171 is the object where is more difficult to trace a symmetric velocity field in its ionised gas component (see Appendix C), the deviation of the maximmum-velocity positions from a straight line is of the order of δPA_{kin} ~90°. In Sec. 5, we discuss the possible relation of δPA_{kin} with the level of bar strength of the non-interacting galaxies.

4.3. Dependence on the measuring radius

In previous sections, to compare the PA_{kin} of both components, we used the same distance to average the polar coordinates of positions defined by the lines of nodes (see Sec. 3). In our data, usually the stellar velocity map limits this distance where the average is done. For barred galaxies, it is similar (and a few times smaller) than half the length of the bar (see r_{bar} in table B.1 and r in tables B.2 B.3). For the majority of the galaxies, the ionised gas extends further out for these galaxies. Our results could therefore be biased because of measuring the average kinematic orientation on a distance similar or close to the bar length.

To study the impact of this distance in the global orientation of the galaxies, we calculated the morpho-kinematic misalignments at different radii in a sub-sample of 49 low-inclined galaxies ($\epsilon < 0.5$). PA_{kin} is computed up to two different radius, r_{out} and r_{in} (see table B.4). The former defines the largest extension of the velocity map in any component. For barred galaxies r_{in} defines the bar length, for non-barred galaxies we define it as half of the r_{out}. $PA_{kin}(r_{out})$ is the average of the polar coordinates from r_{in} to r_{out}, while $PA_{kin}(r_{in})$ is the average from the kinematic centre up to r_{in}.

Left panels of Fig. 4 show, for both components, the morpho-kinematic misalignment respect to the orientation of an ellipse at the outermost region of each galaxy (PA^{out}_{morph}).. Red symbols correspond to misalignments with $PA_{kin}(r_{in})$, while blue ones represent misalignments for $PA_{kin}(r_{out})$). Note that in most of the cases PA^{out}_{morph} is measured at larger radii than $PA_{kin}(r_{out})$. Right panels compare the difference between $PA_{kin}(r_{in})$ and $PA_{kin}(r_{out})$. Figure 4 evidences the similar alignment of the kinematic PA for different morphologies at the different measuring radius, r_{in} and r_{out}, in particular for barred galaxies. On the one hand, the comparison of kinematic PAs and PA^{out}_{morph} (left panels) reveals that 90% of the objects have differences smaller than 16° (20°) for the outer (inner) region in the stellar component. Differences became smaller for the ionised gas (13° and 20° for outer and inner regions, respectively). On the other hand, when we compare PA_{kin} at the inner and outer radii (right panels), we find that 90% of the galaxies have differences smaller than 20° (16°) for the stellar (ionised gas) component. These plots quantify what we observed in velocity fields; at different radii the orientation of the major kinematic PA remains rather constant. Moreover at different radii, PA_{kin} seems to be aligned with the orientation of the major photometric axis rather than other morphological local features such as bars. We find one outlier in both components: the strongly barred late-type galaxy (NGC 171). This galaxy presents the smallest ellipticity in the sample (see Fig. A.2), making difficult to determine a reliable estimation of PA^{out}_{morph}. From these morpho-kinematic differences as well as the differences presented in Sections 4.1 and 4.2 we suggest that for this sample of non-interacting galaxies, the stars and the ionised gas follow the potential of the disk.

5. The impact of bars in velocity maps

Simultaneous comparisons of the stellar and ionised gas resolved kinematics in barred galaxies are rather scarce. Falcón-Barroso et al. (2006) studied those cases found in a sample of 24 spiral bulges. The sample included nine barred galaxies. Kinematic misalignments between the two components for these galaxies ranged from 1° to 38°. A subsequent detailed study of the galaxy NGC 5448 (Fathi et al. 2005) revealed a kinematic misalignment between these two components of 25°. These differences

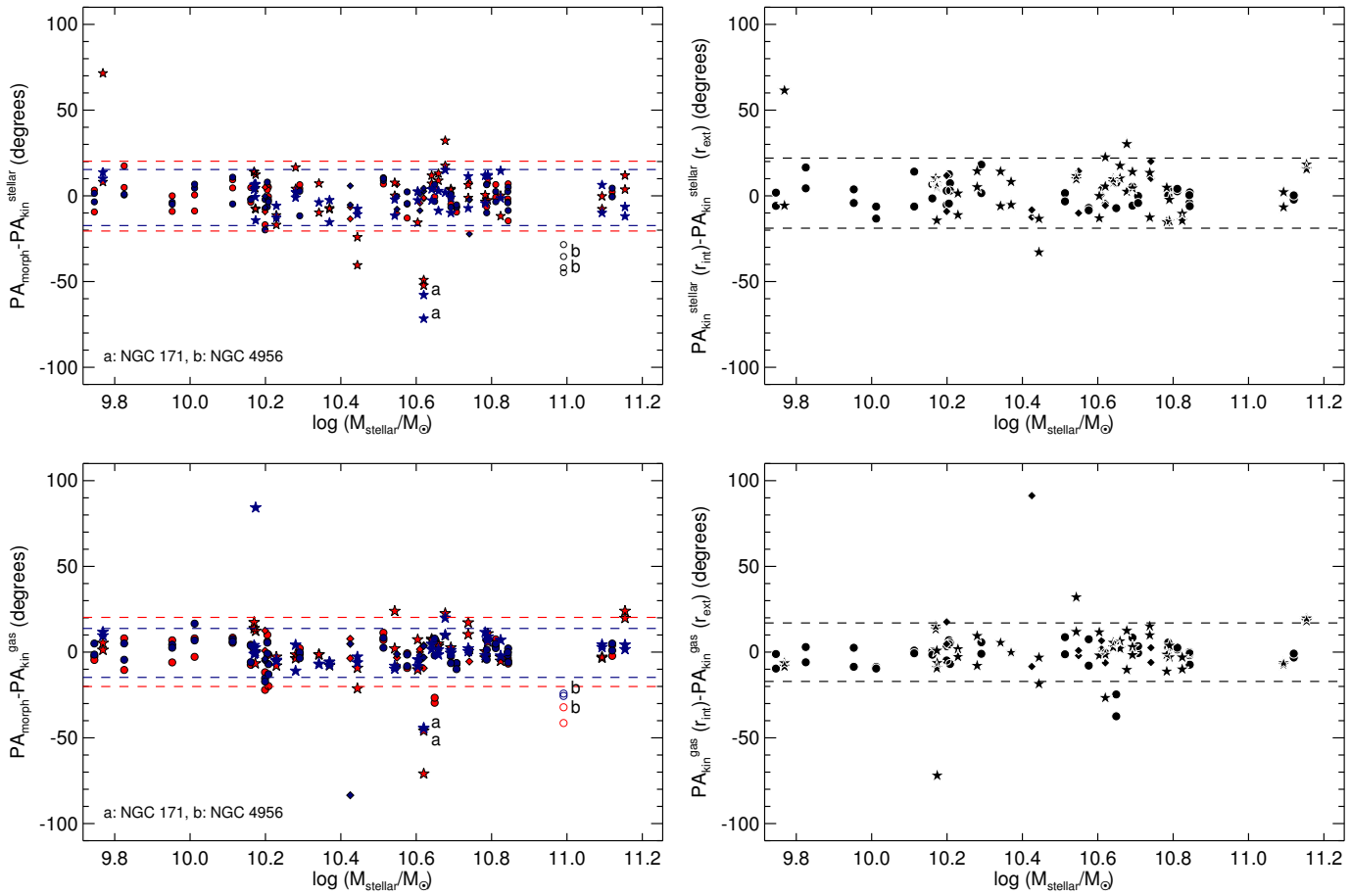

Fig. 4. Left panels: Morpho-kinematic PA misalignments at different regions of the galaxy against the stellar mass for both the stellar (top panel) and the ionised gas (bottom panel) components in a subsample of low-inclined galaxies. In each of these panels, the red points represent the morpho-kinematic PA misalignment between PA^{out}_{morph} (see table B.1) and PA_{kin} at r_{in}. Blue points represent the morpho-kinematic misalignment between PA^{out}_{morph} and PA_{kin} up to r_{out} (see section 4.3 for details). Filled circles, squares and stars represent non-barred, weakly-barred and strongly-barred galaxies, respectively. Right panels: Difference between the kinematic PA derived at r_{in} and r_{out} against the stellar mass for both the stellar (top panel) and the ionised gas (bottom panel) components. In the panels we highlight those objects with larger misalignments.

are explained by the fact that the morphological PA of the galaxies was measured within the same FoV probed by their kinematics (i.e. the inner regions of those galaxies). The PA_{morph} in those cases are thus biased due to the bar. Throughout this study we find that the global kinematic orientation (measured by the major-axis kinematic PA) for the stellar and the ionised gas are aligned for non-interacting objects in the CALIFA survey (see Fig. 2 and 3). This result appears to hold at different radial lengths of the galaxies (Fig. 4), even for barred galaxies. To quantify the departures from perfect axisymmetry in the global kinematic orientation, we plot in top panels of Fig. 5 histograms showing the deviations from a perfect straight line observed in the stellar and ionised-gas kinematic maps ($\delta PA^{stellar}_{kin}$, δPA^{gas}_{kin}). As we already note in Sec. 4.2 the mean value of these deviations is larger for the stellar component in comparison to the ionized gas. For both components the strongly barred galaxies present slightly larger values respect to the non-barred galaxies. In particular the ionised gas component presents a difference between the distribution of barred and non-barred galaxies. This suggest that although the global kinematic orientation is stable in non-interacting galaxies, in particular for barred galaxies, some other kinematic parameters such as δPA^{gas}_{kin} (at higher spatial and spectral resolution as the present velocity fields) can be sensitive to the presence of strong bars.

It is important to note that there is still a fair fraction of strongly barred systems with δPA_{kin} consistent with those observed in non-barred galaxies. We have investigated whether this effect is caused by the flattening of the galaxy,or due to the relative orientation of the bar with respect to the disk major axis. This is shown in the middle and lower panels of Fig. 5. The projected deviation of the kinemtic PA (δPA_{kin}) seems to grow at lower apparent flattening of the galaxy (as a surrogate for inclination). This trend is particular clear for barred galaxies, it may be induced by projections effects. Using the method presented in this study, any kinematic deviation from a straight line would be more easily quantified in a nearly face-on velocity field than in the same field viewed as edge-on. For high inclined galaxies with large kinematic deviations, we may even trace vertical motions rather than radial deviation from a circular velocity field. Note however that other kinematic indicators such as the intrinsic kinematic misalignment do not present a clear trend respect to the ellipticity (see Appendix A). As for the orientation of the bar with respect to the disk major axis, the kinematic deviations covers a wide range of values for a given alignment between the bar and disk orientation, indicating that at least for barred galaxies the orientation of the bar with respect to the disk may not affect drastically the scatter in the location of maximum velocities.

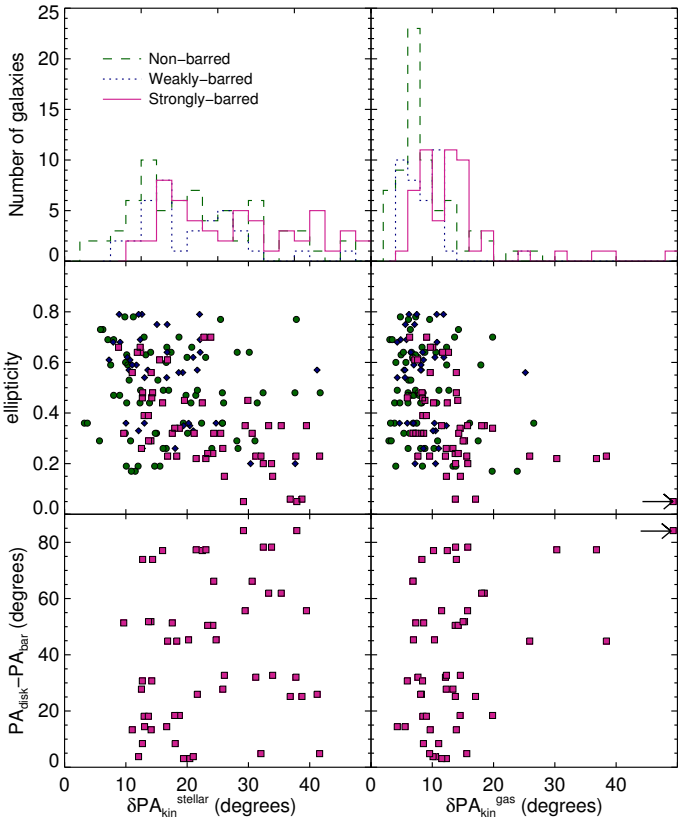

Fig. 5. Top: Histograms of the kinematic departure from a straight line in the velocity maps measured via $\delta PA_{kin}^{stellar}$ (left) and δPA_{kin}^{gas} (right) separated by different bar strengths. Dashed-lines represent the non-barred galaxies, dotted-lines correspond to the weakly-barred galaxies and solid-lines shows the distribution of strong barred galaxies. Middle: Apparent flattening of the galaxies via the ellipticity, as in previous figures, the green-filled circles represent the non-barred galaxies, blue diamonds correspond to weakly-barred galaxies and violet squares represent the barred galaxies. Bottom: Difference between the PA of the disk (PA_{disk}) and the PA of the bar (PA_{bar}) for strongly-barred galaxies only. Arrows in middle and bottom gas panels indicate the galaxy NGC 171 ($\delta PA_{kin}^{gas} \sim 90^\circ$)

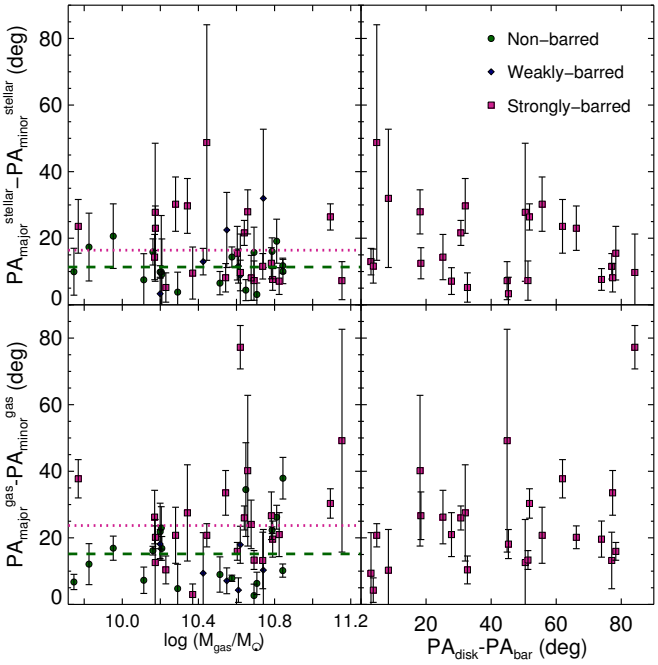

Fig. 6. Misalignment between the major and minor kinematic PA for a subsample of low-inclined galaxies($\epsilon < 0.5$). 0° represents perpendicularity between major and minor axes (see section 5 for details). Left panels show these misalignments as function of the stellar mass for the stellar (top) and the ionised gas (bottom) components. Right panels present these kinematic misalignment as function of the morphological alignment of the bar with respect to the disk for barred galaxies. As in previous figures, the green-filled circles represent the non-barred galaxies, blue diamonds correspond to weakly-barred galaxies and violet squares represent the barred galaxies. Dotted-violet lines represent the mean value for the barred galaxies while dashed-green lines represent the mean value for the non-barred galaxies.

The velocity maps of barred galaxies often show, however, clear signatures of perturbations from a symmetric velocity field (e.g., Hernandez et al. 2005; Fathi et al. 2009). A characteristic "S"-shape in the zero-velocity curve is observed in several of these ionised gas kinematic maps (e.g., Peterson & Huntley 1980; García-Barreto & Rosado 2001; Emsellem et al. 2006). For a pure rotating disk galaxy the major and minor axis are perpendicular everywhere (Binney & Merrifield 1998). To account for the distortion in the zero-curve velocity we estimate the difference between the above kinematic PAs. For each low-inclined galaxy ($\epsilon < 0.5$) we estimate the largest departure among the four kinematic PAs (approaching and receding major PAs and their corresponding minor PAs). 0° represents perpendicularity between major and minor axes. In Fig. 6 we represent these departures against the stellar mass (left panels) and the photometric alignment of the bar respect to the disk for barred galaxies (right panels) for the stellar (top panels) and nebular components (bottom panels). For the stellar component, almost all the low-inclined galaxies present differences smaller than ∼30° except for the barred galaxy NGC 6155. Even more, strongly-barred galaxies spread homogeneously in this range as the non-barred objects. The average departure between strongly and non barred galaxies is similar (∼11° and ∼15°, respectively). The ionised gas component display a wide range of differences between the major and minor kinematic PAs. In particular, strongly-barred galaxies present a wider range of differences than non-barred sample. The average of this difference for the barred galaxies is larger (∼24°) respect to the unbarred galaxies (∼15°). According to numerical simulations, the difference between the major and minor kinematic PA is best seen in velocity fields where the bar makes an angle of 45° with the major axis of the galaxy (e.g., Athanassoula 1984; Scannapieco & Athanassoula 2012). Due to the moderate sub-sample of barred galaxies in this study and the rather large uncertainty in determine the minor kinematic PA, it is not clear weather larger differences in the kinematic PAs are observed at this specific angle between the bar and the disk PA. Note however, that for the stellar component an increment in this difference seems to be present at PA_{disk} - $PA_{bar} \sim 50°$. In the ionised gas, for a given morphological alignment between the bar and the disk we find a broad range of differences between the major and minor kinematic PA. Given the spectral and spatial resolution in our velocities distributions, we consider that the difference between the major and minor kinematic PAs is a sensitive indicator of the presence of a bar in particular for the ionised gas component. Detailed individual studies are required in order to explain the

shape and length of the distortion in this velocity curve as well as to determine if the ionized gas is more sensitive component to the bar potential. These issues are beyond the scope of this study, however our results motivate numerical simulations to address the nature of the kinematics in non-interacting galaxies. As opposed to the previous kinematic indicators (see Fig. 2 and 3) this indicator of kinematic distortion varies significantly for non-interacting galaxies making difficult to use it as a discriminator to distinguish the kinematic distortion produced by the merging event or a secular process.

6. Conclusions

We have studied the stellar and ionised-gas kinematics for a sample of 80 non-interacting galaxies in the CALIFA survey. The fraction of barred and non-barred objects in this sample is similar. We find that for 90% of the sample the global orientation of the stellar and ionised gas is fairly aligned (misalignment smaller than $\sim 20^{\circ}$) with respect to the global photometric orientation of the galaxy, including barred and non-barred objects. From the method used to measure the major kinematic PA we study the internal kinematic PA misalignments namely, the difference between the receding and approaching kinematic PA. We find intrinsic aligned velocity fields in both components for a large fraction of the sample (intrinsic misalignments smaller than 15° degrees for the stellar and the ionised gas components).

We also compared the derived kinematic PA for the stellar and the ionised gas components. We observe a tight alignment (16° degrees of difference) between both components for the majority of this non-interacting sample. This result holds even in barred galaxies when the comparison is carried out either at the radius of the bar or further out, the radius of the disk. From these results we suggest that the global kinematics in non-interacting galaxies in both the stellar and the ionised gas components (measured by the major kinematic position angle) seems to be dominated by the mass of the disk, rather than other morphological component that can induce non-circular patterns in the observed velocity fields such as bars. Even though locally bars can redistribute the angular momentum, energy and mass; the global kinematic pattern that dominates across the galactic disk -including the bar- is consistent with a regular rotational pattern.

We will use the results presented in this paper to gauge the kinematic distortions caused by external forces in galaxies that undergo a merger event in Barrera-Ballesteros et al. (in prep.).

Acknowledgements

We thank the referee for a thorough reading of this work and his/her comments and suggestions. We also thank Lindsay Holmes for allow us to use her DiskFit kinematic modelling for comparison with our results. This study makes use of the data provided by the Calar Alto Legacy Field Area (CALIFA) survey (http://www.califa.caha.es). Based on observations collected at the Centro Astronómico Hispano Alemán (CAHA) at Calar Alto, operated jointly by the Max-Planck-Institut für Astronomie and the Instituto de Astrofísica de Andalucia (CSIC). CALIFA is the first legacy survey performed at the Calar Alto. The CALIFA collaboration would like to thank to the IAA-CSIC and MPIA-MPG as major partners of the observatory, and CAHA itself, for the unique access to the telescope time and support in manpower and infrastructures. The CALIFA collaboration also thanks the CAHA staff for the dedication to this project. J. B.-B. and B. G.-L. thank the support from the Plan Nacional de I+D+i (PNAYA) funding programs (AYA2012-39408-C02-02) of Spanish Ministry of Economy and Competitiveness (MINECO). J. F.-B. acknowledges support from the Ramón y Cajal Program, grants AYA2010-21322-C03-02 from the Spanish Ministry of Economy and Competitiveness (MINECO). We also acknowledge support from the FP7 Marie Curie Actions of the European Commission, via the Initial Training Network DAGAL under REA grant agreement number 289313. R.A.M is funded by the Spanish program of International Campus of Excellence Moncloa (CEI). L. V. M. acknowledges support from the Grant AYA2011-30491-C02-01 co-financed by MICINN and FEDER funds, and the Junta de Andalucia (Spain) grants P08-FQM-4205 and TIC-114. J.I.P. acknowledges financial support from the Spanish MINECO under grant AYA2010-21887-C04-01 and from Junta de Andalucía Excellence Project PEX2011-FQM7058. J.M.A. acknowledges support from the European Research Council Starting Grant (SEDmorph; P.I. V. Wild)

References

Abazajian, K. N., Adelman-McCarthy, J. K., Agüeros, M. A., et al. 2009, ApJS, 182, 543
Aguerri, J. A. L., Méndez-Abreu, J., & Corsini, E. M. 2009, A&A, 495, 491
Athanassoula, E. 1984, Phys. Rep., 114, 319
Athanassoula, E. 2003, MNRAS, 341, 1179
Barazza, F. D., Jogee, S., & Marinova, I. 2008, ApJ, 675, 1194
Barnes, E. I. & Sellwood, J. A. 2003, AJ, 125, 1164
Binney, J. & Merrifield, M. 1998, Galactic Astronomy
Binney, J. & Tremaine, S. 2008, Galactic Dynamics: Second Edition (Princeton University Press)
Cappellari, M. & Copin, Y. 2003, MNRAS, 342, 345
Cappellari, M. & Emsellem, E. 2004, PASP, 116, 138
Cappellari, M., Emsellem, E., Krajnović, D., et al. 2011, MNRAS, 413, 813
Croom, S. M., Lawrence, J. S., Bland-Hawthorn, J., et al. 2012, MNRAS, 421, 872
Debattista, V. P. & Sellwood, J. A. 1998, ApJ, 493, L5
Debattista, V. P. & Sellwood, J. A. 2000, ApJ, 543, 704
Ellison, S. L., Patton, D. R., Simard, L., & McConnachie, A. W. 2008, AJ, 135, 1877
Emsellem, E., Cappellari, M., Peletier, R. F., et al. 2004, MNRAS, 352, 721
Emsellem, E., Fathi, K., Wozniak, H., et al. 2006, MNRAS, 365, 367
Epinat, B., Amram, P., Marcelin, M., et al. 2008, MNRAS, 388, 500
Eskridge, P. B., Frogel, J. A., Pogge, R. W., et al. 2000, AJ, 119, 536
Falcón-Barroso, J., Bacon, R., Bureau, M., et al. 2006, MNRAS, 369, 529
Fathi, K., Beckman, J. E., Piñol-Ferrer, N., et al. 2009, ApJ, 704, 1657
Fathi, K., van de Ven, G., Peletier, R. F., et al. 2005, MNRAS, 364, 773
García-Barreto, J. A. & Rosado, M. 2001, AJ, 121, 2540
García-Lorenzo, B. 2013, MNRAS, 534
Hernandez, O., Carignan, C., Amram, P., Chemin, L., & Daigle, O. 2005, MNRAS, 360, 1201
Hernandez, O., Fathi, K., Carignan, C., et al. 2008, PASP, 120, 665
Husemann, B., Jahnke, K., Sánchez, S. F., et al. 2013, åp, 549, A87
Józsa, G. I. G., Kenn, F., Klein, U., & Oosterloo, T. A. 2007, A&A, 468, 731
Knapen, J. H., Shlosman, I., & Peletier, R. F. 2000, ApJ, 529, 93
Krajnović, D., Cappellari, M., de Zeeuw, P. T., & Copin, Y. 2006, MNRAS, 366, 787
Krajnović, D., Emsellem, E., Cappellari, M., et al. 2011, MNRAS, 414, 2923
Kronberger, T., Kapferer, W., Unterguggenberger, S., Schindler, S., & Ziegler, B. L. 2008, A&A, 483, 783
Kutdemir, E., Ziegler, B. L., Peletier, R. F., et al. 2008, A&A, 488, 117
Marinova, I., Jogee, S., Bacon, D., et al. 2007, in Bulletin of the American Astronomical Society, Vol. 39, American Astronomical Society Meeting Abstracts, 905
Martinez-Valpuesta, I., Shlosman, I., & Heller, C. 2006, ApJ, 637, 214
Menéndez-Delmestre, K., Sheth, K., Schinnerer, E., Jarrett, T. H., & Scoville, N. Z. 2007, ApJ, 657, 790
Moreno, J., Bluck, A. F. L., Ellison, S. L., et al. 2013, MNRAS
Naab, T. & Burkert, A. 2003, ApJ, 597, 893
Nicholson, R. A., Bland-Hawthorn, J., & Taylor, K. 1992, ApJ, 387, 503
Peterson, C. J. & Huntley, J. M. 1980, ApJ, 242, 913
Roth, M. M., Kelz, A., Fechner, T., et al. 2005, PASP, 117, 620
Rozas, M., Relaño, M., Zurita, A., & Beckman, J. E. 2002, A&A, 386, 42
Sánchez, S. F., Kennicutt, R. C., Gil de Paz, A., et al. 2012, åp, 538, A8
Scannapieco, C. & Athanassoula, E. 2012, MNRAS, 425, L10

Scannapieco, C., Gadotti, D. A., Jonsson, P., & White, S. D. M. 2010, MNRAS, 407, L41
Schoenmakers, R. H. M., Franx, M., & de Zeeuw, P. T. 1997, MNRAS, 292, 349
Sellwood, J. A. 2006, ApJ, 637, 567
Sellwood, J. A. 2013, Dynamics of Disks and Warps, ed. T. D. Oswalt & G. Gilmore, 923
Sellwood, J. A. & Debattista, V. P. 2006, ApJ, 639, 868
Sofue, Y. & Rubin, V. 2001, ARA&A, 39, 137
Spekkens, K. & Sellwood, J. A. 2007, ApJ, 664, 204
Thielheim, K. O. & Wolff, H. 1982, MNRAS, 199, 151
Valdes, F., Gupta, R., Rose, J. A., Singh, H. P., & Bell, D. J. 2004, ApJS, 152, 251
Varela, J., Moles, M., Márquez, I., et al. 2004, A&A, 420, 873
Verdes-Montenegro, L., Sulentic, J., Lisenfeld, U., et al. 2005, A&A, 436, 443
Verley, S., Leon, S., Verdes-Montenegro, L., et al. 2007, A&A, 472, 121
Villa-Vargas, J., Shlosman, I., & Heller, C. 2009, ApJ, 707, 218
Weinberg, M. D. 1985, MNRAS, 213, 451

[1] Instituto de Astrofísica de Canarias, Calle Vía Lactéa s/n, E-38205, Spain
[2] Departamento de Astrofísica, Universidad de La Laguna (ULL), E-38200 La Laguna, Tenerife, Spain
[3] Max-Planck Institute for Astronomy, Königstul 17, 69117 Heidelberg, Germany
[4] School of Physics and Astronomy, University of St Andrews, North Haugh, St Andrews, KY16 9SS, UK
[5] Department of Physics, Royal Military Collage of Canada, PO Box 17000, Station Forces, Kingston, Ontario, K7K7B4, Canada
[6] Instituto de Astrofísica de Andalucía (CSIC), Glorieta de la Astronomía S/N, 18008 Granada, Spain
[7] Instituto de Astronomía, Universidad Nacional Autonóma de Mexico, A.P. 70-264, 04510, México,D.F.
[8] Centro Astronómico Hispano Alemán de Calar Alto (CSIC-MPG), C/ Jesús Durbán Remón 2-2, 4004 Almería, Spain.
[9] European Southern Observatory, ESO Headquarters, Karl-Schwarzschild-Str. 2, 85748 Garching b. München, Germany
[10] Leibniz-Institut für Astrophysik Potsdam (AIP), An der Sternwarte 16, 14482, Potsdam, Germany
[11] CEI Campus Moncloa, UCM-UPM, Departamento de Astrofísica y CC. de la Atmósfera, Facultad de CC. Físicas, Universidad Complutense de Madrid, Avda. Complutense S/N, 28040 Madrid, Spain
[12] University of Vienna, Departament of Astrophysics, Türkenschanzstr. 17, 1180 Vienna, Austria
[13] Department of Physics & Astronomy, University of Missouri-Kansas City, 5110 Rockhill Road, Kansas City, MO, USA
[14] Sydney Institute for Astronomy, School of Physics A28, University of Sydney, NSW 2006, Australia

Appendix A: Kinematic alignments versus apparent ellipticity

All the kinematic parameters presented in this study are determined on the plane of the sky. Therefore, it is expected that any intrinsic kinematic property would be affected by the inclination of the galaxy with respect to the plane of the sky. In this appendix we show the same kinematic misalignments presented in section 4 with respect to the apparent ellipticity as proxy of the apparent inclination of the galaxies.

In Figure A.1 we plot the distribution of the non-interacting galaxies with respect to the ellipticity. We have a fair coverage of galaxies at different inclinations , in particular for the low-inclined ones ($\epsilon < 0.5$). In order to have consistent results, we also try to have the same fraction of barred vs unbarred galaxies at different ellipticity bins.

In Figure A.2 we plot the morpho-kinematic misalignments explained in section 4.1 against the ellipticity for both components as well as the internal kinematic misalignment in each component (Fig. A.3) and the comparison of the kinematic PA between the stars and the gas (Fig. A.4). We find large morpho-kinematic misalignments in galaxies with low ellipticities ($\epsilon < 0.3$, see Fig. A.2).

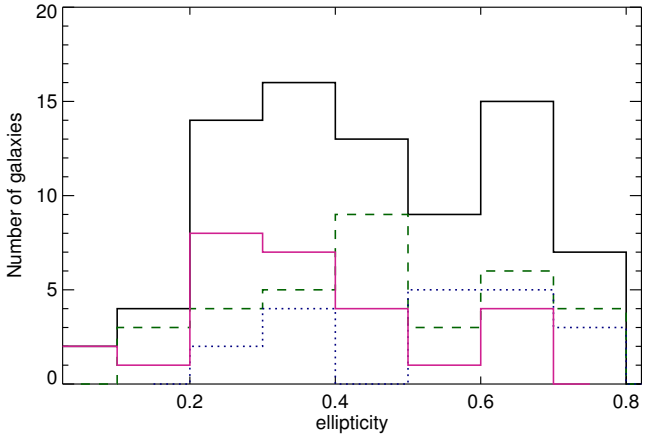

Fig. A.1. Distribution of the ellipticity as proxy of the inclination for the galaxies used in this study. Dashed-lines represent the non-barred galaxies, dotted-lines correspond to the weakly-barred galaxies and solid-lines shows the distribution of strong barred galaxies.

For the kinematic parameters independent of the morphology (i.e., Figs. A.3 and A.4), we find rather similar values at different ellipticity bins. In each panel of these figures we plot an estimation of the projections effects as function of the ellipticity assuming a face-on misalignment of 60° (see Fig. A.2) in any of the (morpho-) kinematic indicators. This value was chosen to approximately match the misalignments found at large ellipticities. Within uncertainties all the galaxies display internal kinematic misalignments smaller as the ones expected for their inclinations. In other words for these misalignments we do not find large scatters at low ellipticities as expected for a quantity heavily affected by projection effects.

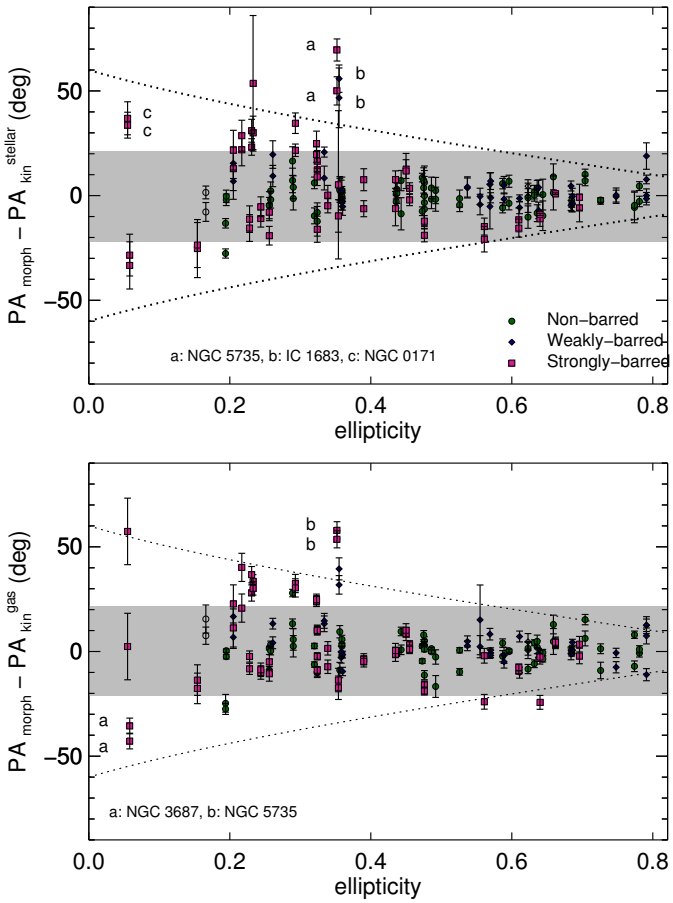
PA morph − PA kin stellar (deg)
PA morph − PA kin gas (deg)
ellipticity
a: NGC 5735, b: IC 1683, c: NGC 0171
a: NGC 3687, b: NGC 5735
Non−barred
Weakly−barred
Strongly−barred

Fig. A.2. Difference between the morphological PA (PA_{morph}) and the kinematic PA (PA_{kin}) against the ellipticity of the outermost isophote of the galaxy for the stars (top panel) and the ionised gas (bottom panel). Both kinematic sides of the velocity maps were compared with PA_{morph}. In each panel, the green-filled circles represent the non-barred galaxies, blue diamonds are weakly-barred galaxies and violet squares correspond to barred galaxies. For early-type galaxies we use empty circles. Labels indicate the 3-σ outliers. Dashed lines represent the projection effect of a morpho-kinematic misalignment of 60° measured in the plane of the galaxy. In each panel, the grey area represents the 2σ dispersion of the sample.

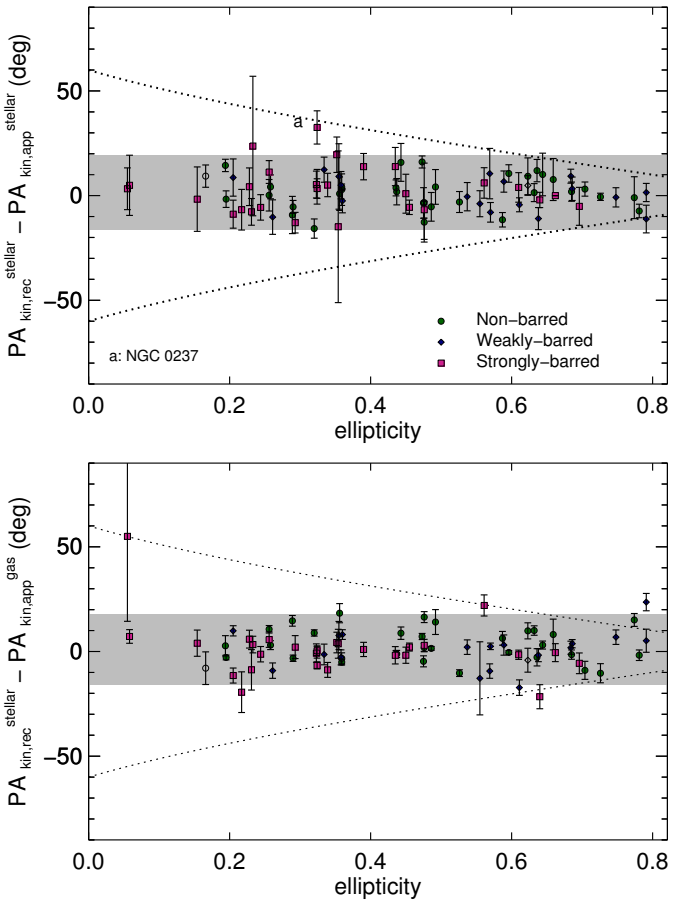

Fig. A.3. Internal kinematic misalignment between the receding PA ($PA_{kin,rec}$) and approaching ($PA_{kin,app}$) kinematic position angle against the ellipticity. In each panel the green-filled circles represent the non-barred galaxies, blue diamonds correspond to weakly-barred galaxies and violet squares represent the barred galaxies. Empty circles represent the early-type galaxies. Labels indicate the 3-σ outlier. Dashed lines represent the projection effect of a morpho-kinematic misalignment of 60° measured in the plane of the galaxy. In each panel, the grey area represents the 2σ dispersion of the sample.

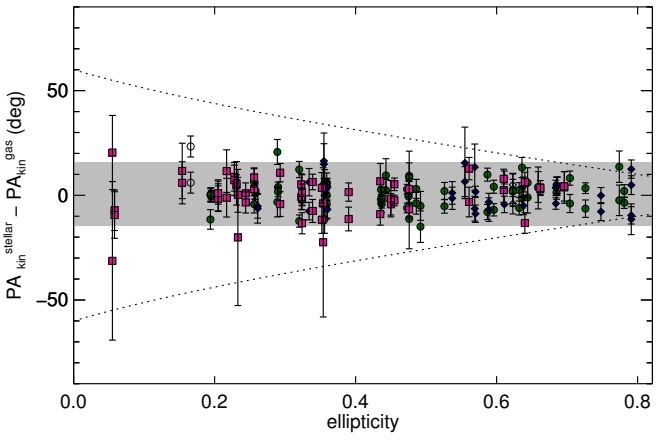

Fig. A.4. Stellar and ionised gas difference respect the ellipticity. the green-filled circles represent the non-barred galaxies, blue diamonds correspond to weakly-barred galaxies and violet squares represent the barred galaxies. Empty circles represent the early-type galaxies. Dashed lines represent the projection effect of a morpho-kinematic misalignment of 60° measured in the plane of the galaxy. In each panel, the grey area represents the 2σ dispersion of the sample.

Appendix B: Tables

Table B.1. Morphological parameters of the sample of non-interacting CALIFA galaxies used in this study.

CALIFA id	Name	Morphological type	Bar strength	ϵ	PA^{out}_{morph} (°)	PA_{bar} (°)	r_{bar} (arcsec)	Stellar mass $\log(M/M_\odot)$
(1)	(2)	(3)	(4)	(5)	(6)	(7)	(8)	(9)
1	IC5376	Sb	A	0.69	50	...	...	10.57
2	UGC00005	Sbc	A	0.53	50	...	...	10.72
7	UGC00036	Sab	AB	0.61	50	...	...	10.88
8	NGC0001	Sbc	A	0.32	50	...	...	10.71
10	NGC0036	Sb	B	0.48	50	128	12	10.79
23	NGC0171	Sb	B	0.05	50	122	33	10.62
25	NGC0180	Sb	B	0.34	50	147	22	10.78
28	NGC0214	Sbc	AB	0.26	50	59	14	10.74
30	NGC0237	Sc	B	0.32	50	40	7	10.17
31	NGC0234	Sc	AB	0.20	50	...	...	10.55
33	NGC0257	Sc	A	0.36	50	...	...	10.69
41	UGC00841	Sbc	A	0.77	50	...	...	9.71
43	IC1683	Sb	AB	0.35	50	168	8	10.43
53	UGC01057	Sc	AB	0.69	50	...	...	10.11
108	NGC1093	Sbc	B	0.39	50	117	10	10.66
116	UGC02405	Sbc	A	0.66	50	...	...	10.40
131	NGC1542	Sab	AB	0.59	50	...	...	10.30
147	NGC2253	Sbc	B	0.32	50	...	...	10.37
149	NGC2347	Sbc	AB	0.36	50	...	...	10.62
151	NGC2410	Sb	AB	0.68	50	...	...	10.78
152	UGC03944	Sbc	AB	0.57	50	94	5	9.87
153	UGC03969	Sb	A	0.78	50	...	...	10.61
273	IC2487	Sc	AB	0.79	50	...	...	10.29
275	NGC2906	Sbc	A	0.44	50	...	...	10.29
277	NGC2916	Sbc	A	0.36	50	...	...	10.65
307	UGC05359	Sb	B	0.70	50	...	...	10.54
364	UGC06036	Sa	A	0.73	50	...	...	11.09
386	UGC06312	Sab	A	0.64	50	...	...	10.93
414	NGC3687	Sb	B	0.06	50	174	14	10.17
436	NGC3811	Sbc	B	0.23	50	22	24	10.34
489	NGC4047	Sbc	A	0.26	50	...	...	10.58
515	NGC4185	Sbc	AB	0.33	50	167	20	10.61
518	NGC4210	Sb	B	0.24	50	47	17	10.17
580	NGC4711	Sbc	A	0.47	50	...	...	10.20
602	NGC4956	E1	A	0.17	50	...	...	10.99
610	UGC08267	Sb	AB	0.75	50	...	...	10.68
624	NGC5157	Sab	B	0.23	50	138	21	11.15
630	NGC5205	Sbc	B	0.35	50	108	12	9.77
664	UGC08778	Sb	A	0.70	50	...	...	10.15
684	NGC5406	Sb	B	0.29	50	56	20	11.09
714	UGC09067	Sbc	AB	0.54	50	27	5	10.36
715	NGC5520	Sbc	A	0.49	50	...	...	9.75
743	NGC5622	Sbc	A	0.48	50	...	...	10.11
748	NGC5633	Sbc	A	0.26	50	...	...	10.16
753	NGC5656	Sb	A	0.19	50	...	...	10.51
764	NGC5720	Sbc	B	0.44	50	60	7	10.74
768	NGC5732	Sbc	A	0.48	50	...	...	9.83
771	NGC5735	Sbc	B	0.35	50	94	20	10.28
777	NGC5772	Sab	A	0.44	50	...	...	10.84
779	UGC09598	Sbc	AB	0.64	50	...	...	10.45
782	UGC09629	E7	AB	0.62	50	...	...	11.02

Notes. (1) CALIFA ID number. (2) name of the galaxy. (3) morphological type from visual clasification (see Walcher et. al in preparation for details). (4) bar strength of the galaxy from the same morphological visual clasification (see Walcher et. al. in preparation for details). (5) and (6) ellipticity (ϵ) and position angle (PA^{out}_{morph}) from an ellipse fitting at the largest scale isophote of the SDSS r-band image. Both measurements were inferred using the IRAF task *ellipse*. (7) and (8) position angle (PA_{bar}) and length of the bar (r_{bar}) derived from an ellipse fitting on the SDSS r-band image. (9) stellar masses (see Walcher et. al in preparation for details).

Table B.1. continue

CALIFA id	Name	Morphological type	Barredness	ϵ	PA^{out}_{morph} (°)	PA_{bar} (°)	r_{bar} (arcsec)	Stellar mass $\log(M/M_\odot)$
(1)	(2)	(3)	(4)	(5)	(6)	(7)	(8)	(9)
790	UGC09777	Sbc	A	0.49	50	...	...	10.21
791	NGC5908	Sa	A	0.36	50	...	...	11.12
804	NGC5971	Sb	AB	0.56	50	...	...	10.22
810	NGC5980	Sbc	A	0.60	50	...	...	10.62
813	NGC6004	Sbc	B	0.20	50	15	16	10.60
823	NGC6063	Sbc	A	0.44	50	...	...	9.95
824	IC1199	Sb	AB	0.57	50	...	...	10.20
826	NGC6081	S0a	A	0.59	50	...	...	11.04
831	NGC6132	Sbc	A	0.64	50	...	...	10.15
834	UGC10380	Sb	AB	0.79	50	...	...	10.92
836	NGC6155	Sc	A	0.29	50	...	...	10.01
842	NGC6186	Sb	B	0.23	50	54	35	10.44
853	NGC6361	Sab	A	0.29	50	...	...	10.81
854	UGC10811	Sb	B	0.66	50	...	...	10.75
856	IC1256	Sb	AB	0.36	50	130	7	10.20
857	NGC6394	Sbc	B	0.64	50	...	...	10.79
862	NGC6478	Sc	A	0.63	50	...	...	10.90
869	NGC6941	Sb	B	0.26	50	108	16	10.82
872	UGC11649	Sab	B	0.22	50	162	17	10.54
876	NGC7047	Sbc	B	0.45	50	115	20	10.68
886	NGC7311	Sa	A	0.47	50	...	...	10.84
887	NGC7321	Sbc	B	0.32	50	62	10	10.69
889	NGC7364	Sab	A	0.32	50	...	...	10.79
890	UGC12185	Sb	B	0.56	50	139	22	10.58
896	NGC7466	Sbc	A	0.62	50	...	...	10.70
904	NGC7591	Sbc	B	0.46	50	1	11	10.64
924	NGC7716	Sb	A	0.19	50	...	...	10.20
929	UGC12810	Sbc	B	0.61	50	...	...	10.61
938	NGC5947	Sbc	B	0.15	50	26	11	10.23

Table B.2. Stellar Kinematic properties of the non-interacting sample selected for this study included in the CALIFA survey.

id	$\Delta\alpha$	$\Delta\delta$	V_{sys}	r_{max}	r_{min}	PA_{morph} (r_{max})	PA approaching		PA receding	
							PA_{kin}	δPA_{kin}	PA_{kin}	δPA_{kin}
	(arcsec)	(arcsec)	(km s^{-1})	(arcsec)	(arcsec)	(°)	(°)	(°)	(°)	(°)
(1)	(2)	(3)	(4)	(5)	(6)	(7)	(8)	(9)	(10)	(11)
1	0.6 ± 0.6	1.7 ± 0.5	4963 ± 9	22	–	3.7 ± 0.4	6.0 ± 3.3	7.1 ± 2.2	8.2 ± 3.2	8.0 ± 1.8
2	...	...	7209 ± 1	22	–	45.2 ± 0.9	49.9 ± 2.7	10.5 ± 2.7	45.0 ± 0.2	15.2 ± 2.7
7	...	...	6238 ± 1	20	–	17.4 ± 0.2	22.7 ± 2.8	10.7 ± 2.3	18.8 ± 1.6	7.3 ± 1.8
8	-0.6 ± 0.5	-1.1 ± 0.6	4515 ± 9	20	7	106.0 ± 1.1	114.6 ± 4.2	15.0 ± 4.9	118.2 ± 6.2	20.1 ± 3.7
10	...	...	5939 ± 1	25	10	179.3 ± 0.6	19.4 ± 2.7	14.4 ± 2.1	12.0 ± 2.3	12.7 ± 2.4
23	0.4 ± 0.5	-1.0 ± 0.6	3857 ± 1	20	10	126.0 ± 0.7	88.8 ± 7.2	29.2 ± 7.6	92.0 ± 4.9	37.9 ± 10.2
25	0.4 ± 0.5	-0.7 ± 0.4	5204 ± 6	30	7	167.1 ± 1.0	168.1 ± 4.0	18.7 ± 3.0	172.0 ± 3.8	18.0 ± 3.4
28	0.2 ± 0.5	0.2 ± 0.7	4500 ± 12	12	5	60.4 ± 0.8	51.3 ± 5.4	12.7 ± 4.7	40.2 ± 6.3	18.0 ± 4.9
30	...	...	4142 ± 1	20	7	177.3 ± 0.8	17.0 ± 5.8	24.3 ± 5.8	165.3 ± 5.2	30.6 ± 7.4
31	1.9 ± 0.7	-1.1 ± 0.8	4391 ± 6	30	5	82.2 ± 4.9	66.5 ± 7.3	37.6 ± 5.5	76.4 ± 6.7	30.3 ± 9.4
33	-1.1 ± 0.7	1.2 ± 0.8	5183 ± 12	20	7	93.7 ± 1.5	91.0 ± 6.3	25.7 ± 5.6	94.4 ± 4.8	25.8 ± 7.6
41	1.3 ± 0.5	-1.4 ± 0.6	5524 ± 9	15	–	53.9 ± 0.2	58.6 ± 7.1	37.8 ± 9.9	60.3 ± 5.1	25.4 ± 7.5
43	...	...	4839 ± 9	12	7	156.4 ± 1.0	19.0 ± 9.7	20.4 ± 8.1	31.8 ± 7.2	19.4 ± 6.4
53	-0.8 ± 0.5	0.1 ± 0.6	6294 ± 12	20	–	152.2 ± 0.5	152.6 ± 4.7	22.1 ± 4.7	155.1 ± 3.8	12.4 ± 2.9
108	...	...	5224 ± 1	20	5	96.5 ± 1.2	92.9 ± 3.0	13.0 ± 5.0	101.4 ± 1.8	13.7 ± 4.2
116	-0.8 ± 0.4	0.1 ± 0.8	7676 ± 21	10	–	172.4 ± 1.4	164.5 ± 6.3	20.8 ± 7.8	171.7 ± 7.2	16.7 ± 7.1
131	0.2 ± 0.5	-1.8 ± 0.6	3689 ± 10	18	–	128.0 ± 0.4	123.4 ± 3.6	11.7 ± 2.6	129.2 ± 2.8	11.0 ± 2.7
147	...	...	3549 ± 0	25	7	141.7 ± 1.9	117.0 ± 5.7	25.5 ± 3.5	122.1 ± 3.3	21.1 ± 5.0
149	-0.3 ± 0.5	-0.0 ± 0.4	4396 ± 12	20	5	3.9 ± 0.8	8.5 ± 4.3	13.0 ± 3.1	7.2 ± 4.0	10.0 ± 3.7
151	1.4 ± 0.5	0.5 ± 0.5	4662 ± 9	29	–	37.0 ± 0.3	32.4 ± 2.5	9.1 ± 1.8	41.7 ± 2.3	7.9 ± 1.4
152	0.6 ± 0.6	1.3 ± 0.7	3881 ± 9	20	–	121.9 ± 0.5	116.9 ± 5.9	21.7 ± 5.3	125.2 ± 10.0	41.2 ± 14.8
153	-3.1 ± 0.7	-1.6 ± 0.8	7984 ± 18	20	–	134.9 ± 0.3	137.7 ± 2.2	11.2 ± 3.0	130.2 ± 2.4	9.8 ± 3.8
273	1.3 ± 0.7	1.9 ± 0.8	4326 ± 11	33	–	162.9 ± 0.2	162.6 ± 2.7	12.6 ± 2.1	164.5 ± 2.5	12.1 ± 2.3
275	-1.0 ± 0.4	-0.3 ± 0.4	2169 ± 5	27	5	82.1 ± 0.6	79.6 ± 4.6	13.9 ± 2.6	80.2 ± 4.9	20.6 ± 4.6
277	-0.3 ± 0.4	-0.8 ± 0.5	3690 ± 6	25	9	22.3 ± 0.7	19.7 ± 5.9	22.4 ± 3.4	19.6 ± 6.4	19.4 ± 2.9
307	...	...	8344 ± 16	15	–	95.2 ± 0.5	101.8 ± 6.3	23.9 ± 13.3	95.5 ± 5.6	22.7 ± 7.2
364	...	...	6474 ± 1	25	–	99.8 ± 0.4	102.6 ± 1.4	6.2 ± 0.8	101.8 ± 0.8	5.9 ± 1.0
386	0.5 ± 0.6	0.4 ± 0.5	6297 ± 10	17	–	48.9 ± 0.9	44.9 ± 3.9	14.0 ± 3.2	58.1 ± 4.7	17.4 ± 3.9
414	...	...	2521 ± 0	25	7	107.9 ± 3.2	135.6 ± 12.8	36.8 ± 7.8	141.5 ± 11.0	38.7 ± 6.4
436	0.3 ± 0.7	0.5 ± 0.7	3106 ± 9	20	5	24.3 ± 1.1	145.1 ± 39.0	31.2 ± 8.0	173.2 ± 5.9	37.8 ± 11.5
489	-0.2 ± 0.4	-0.9 ± 0.7	3392 ± 5	25	10	104.1 ± 1.0	102.4 ± 3.7	16.6 ± 3.9	106.6 ± 3.8	16.1 ± 3.4
515	...	...	3868 ± 1	25	10	0.2 ± 1.1	159.5 ± 2.3	12.1 ± 3.0	171.8 ± 5.4	21.0 ± 3.1
518	...	...	2712 ± 0	30	5	88.5 ± 1.0	99.2 ± 4.4	24.2 ± 3.5	93.0 ± 3.5	23.4 ± 4.4
580	...	...	4082 ± 1	23	5	43.3 ± 0.5	40.6 ± 4.4	21.4 ± 3.9	36.1 ± 5.1	19.8 ± 3.7
602	-0.4 ± 0.2	-1.0 ± 0.3	4737 ± 5	15	–	75.2 ± 0.8	72.9 ± 3.2	11.5 ± 3.0	82.4 ± 4.4	10.9 ± 4.7
610	1.4 ± 0.8	-1.2 ± 1.0	7125 ± 19	20	–	39.4 ± 0.3	40.2 ± 3.2	16.7 ± 5.0	38.7 ± 3.6	15.1 ± 4.5
624	0.5 ± 0.4	0.5 ± 0.3	7255 ± 7	25	6	116.4 ± 1.5	92.9 ± 3.5	18.3 ± 2.8	85.2 ± 4.8	16.8 ± 3.2
630	...	...	1768 ± 1	20	9	146.4 ± 0.7	157.6 ± 8.0	35.3 ± 8.0	170.1 ± 7.6	33.3 ± 6.5
664	...	...	3220 ± 0	25	–	118.7 ± 0.2	109.4 ± 2.6	13.0 ± 2.0	111.5 ± 2.9	18.7 ± 2.7
684	-1.5 ± 0.3	-0.2 ± 0.3	5331 ± 6	27	7	141.2 ± 2.1	119.9 ± 2.3	14.1 ± 2.5	107.5 ± 4.6	13.7 ± 2.6
714	0.4 ± 0.7	-0.4 ± 0.6	7793 ± 18	20	–	16.7 ± 0.5	12.7 ± 5.0	13.0 ± 2.9	13.0 ± 4.3	16.7 ± 4.1
715	-0.7 ± 0.8	0.0 ± 0.7	1885 ± 9	30	7	66.5 ± 0.4	68.7 ± 3.9	17.0 ± 3.4	62.4 ± 5.0	21.7 ± 3.6
743	-0.1 ± 0.6	1.3 ± 0.7	3868 ± 8	25	5	85.9 ± 0.5	92.1 ± 7.5	32.4 ± 5.2	81.0 ± 6.4	25.7 ± 6.5
748	0.3 ± 0.7	-0.4 ± 0.4	2355 ± 4	25	10	192.5 ± 0.5	17.8 ± 6.2	24.0 ± 4.8	17.6 ± 4.1	28.3 ± 6.3
753	-0.3 ± 0.4	-0.5 ± 0.5	3175 ± 4	25	7	56.1 ± 0.6	57.4 ± 3.0	15.6 ± 2.8	57.0 ± 3.2	10.1 ± 1.8
764	1.0 ± 0.7	-1.1 ± 0.8	7704 ± 11	20	7	128.4 ± 0.7	121.3 ± 4.0	16.0 ± 4.8	136.1 ± 7.8	22.5 ± 4.2
768	-1.0 ± 0.5	-0.2 ± 0.6	3735 ± 8	15	7	42.4 ± 0.9	50.0 ± 20.6	37.6 ± 12.1	41.7 ± 13.8	41.7 ± 7.4
771	-1.1 ± 0.8	-1.8 ± 0.9	3762 ± 9	20	7	98.7 ± 0.9	29.5 ± 6.6	29.5 ± 7.6	46.5 ± 9.7	39.5 ± 14.3
777	0.5 ± 0.4	-1.0 ± 0.4	4836 ± 9	30	10	36.1 ± 0.4	35.7 ± 2.0	10.1 ± 1.6	38.4 ± 3.1	12.3 ± 1.9
779	-1.8 ± 0.5	-1.1 ± 0.6	5527 ± 8	23	–	121.8 ± 0.3	129.4 ± 4.4	22.1 ± 5.0	117.9 ± 3.7	16.7 ± 5.7
782	0.9 ± 0.3	0.9 ± 0.3	7803 ± 10	12	–	152.9 ± 0.5	147.6 ± 3.0	10.3 ± 3.3	152.9 ± 3.6	21.0 ± 8.2

Notes. (1) CALIFA identifier. (2) and (3) Location of the kinematic centre. The value listed is the gradient peak (GP) with respect to the optical nucleus (ON) if not, ON is used as kinematic centre (see section 3 for details). (4) Systemic velocity derived from integrated the velocities in a 2.7″ aperture centred in the kinematic centre. (5) Radius used to average the polar coordinates of the positions from the lines of nodes (see section 3 for details). (6) Radius used to average the polar coordinates of the positions from the cero-velocity line (see section 3 for details). (7) Morphological PA inferred by fitting an elipse to an isophote at radius r_{max} in the r-band SDSS image. (8) Kinematic position angle at radius r for the approaching side (see section 3 for details). (9) Standard deviation of the kinematic position angle of the approaching side (see section 3 for details). (10) Kinematic position angle at radius r for the receding side. (11) Standard deviation of the kinematic position angle of the receding side. Values in parenthesis for each row represent the errors obtained from Monte Carlo simulations.

Table B.2. continue B.2

id	$\Delta\alpha$	$\Delta\delta$	V_{sys}	r_{max}	r_{min}	PA_{morph} (r_{max})	PA approaching		PA receding	
							PA_{kin}	δPA_{kin}	PA_{kin}	δPA_{kin}
	(arcsec)	(arcsec)	(km s^{-1})	(arcsec)	(arcsec)	(°)	(°)	(°)	(°)	(°)
(1)	(2)	(3)	(4)	(5)	(6)	(7)	(8)	(9)	(10)	(11)
790	...	...	4677 ± 1	12	5	143.6 ± 1.3	142.4 ± 5.6	16.1 ± 4.3	144.5 ± 5.9	12.4 ± 4.5
791	1.2 ± 0.3	0.4 ± 0.3	3316 ± 5	30	–	152.3 ± 0.3	149.7 ± 1.2	3.2 ± 0.7	154.5 ± 1.3	3.7 ± 0.6
804	-2.2 ± 0.5	-0.5 ± 0.5	3388 ± 7	15	–	126.8 ± 0.5	130.5 ± 4.4	19.3 ± 4.8	127.7 ± 4.7	18.6 ± 5.8
810	-0.3 ± 0.5	-0.1 ± 0.5	4117 ± 9	25	–	15.3 ± 0.5	8.6 ± 3.0	10.0 ± 2.4	19.6 ± 3.1	16.6 ± 3.0
813	...	...	3836 ± 1	28	7	113.1 ± 8.8	101.1 ± 5.5	33.8 ± 5.3	90.0 ± 4.4	32.4 ± 6.1
823	...	...	2838 ± 1	25	7	159.2 ± 0.6	152.2 ± 4.5	31.4 ± 6.5	168.5 ± 7.8	26.0 ± 4.3
824	-0.4 ± 0.5	-1.7 ± 0.6	4730 ± 14	27	–	159.8 ± 0.2	161.6 ± 3.0	10.5 ± 1.8	152.7 ± 4.0	13.6 ± 2.2
826	-0.4 ± 0.5	-1.2 ± 0.5	5070 ± 9	25	–	127.9 ± 0.3	133.4 ± 2.3	10.3 ± 2.2	122.5 ± 2.2	7.5 ± 1.3
831	-0.3 ± 0.8	0.4 ± 0.7	4957 ± 12	15	–	123.4 ± 0.6	123.8 ± 9.4	30.1 ± 9.9	133.8 ± 7.1	28.2 ± 8.4
834	...	...	8694 ± 1	15	–	114.2 ± 0.5	106.3 ± 1.9	8.9 ± 2.6	95.0 ± 5.8	22.0 ± 3.4
836	0.6 ± 0.8	0.8 ± 0.8	2424 ± 4	29	–	148.9 ± 0.9	140.5 ± 5.3	28.1 ± 7.3	133.4 ± 6.1	31.1 ± 5.0
842	0.3 ± 0.5	-2.2 ± 0.5	2970 ± 6	30	7	54.7 ± 0.4	66.9 ± 5.6	41.6 ± 4.5	70.4 ± 5.3	32.0 ± 4.6
853	...	...	3788 ± 1	30	10	53.0 ± 5.0	53.6 ± 2.9	10.8 ± 2.1	49.5 ± 2.2	5.7 ± 1.4
854	...	...	8625 ± 1	20	–	90.9 ± 0.4	90.0 ± 4.3	8.8 ± 3.0	90.0 ± 4.5	12.3 ± 2.9
856	...	...	4696 ± 1	22	5	91.6 ± 0.7	90.0 ± 4.3	24.7 ± 7.1	93.7 ± 3.7	20.2 ± 3.9
857	...	...	8453 ± 1	15	–	36.1 ± 0.4	47.8 ± 3.9	12.4 ± 3.5	45.0 ± 0.2	11.9 ± 2.8
862	...	...	6704 ± 1	25	–	32.1 ± 0.4	30.2 ± 3.4	13.2 ± 2.1	31.7 ± 2.2	10.1 ± 1.9
869	-0.6 ± 0.5	0.9 ± 0.5	6157 ± 7	22	7	121.8 ± 1.8	130.8 ± 4.2	25.8 ± 3.8	141.4 ± 3.9	12.5 ± 2.8
872	-0.2 ± 0.7	-1.3 ± 0.7	3767 ± 11	20	7	85.4 ± 3.0	64.2 ± 6.3	21.5 ± 3.8	56.3 ± 6.9	23.1 ± 4.3
876	-0.6 ± 0.8	1.4 ± 0.8	5740 ± 13	20	5	106.9 ± 1.3	94.2 ± 4.6	19.6 ± 5.0	95.6 ± 9.2	29.9 ± 5.4
886	-1.4 ± 0.3	-0.1 ± 0.2	4488 ± 5	27	7	12.8 ± 0.3	4.2 ± 1.8	8.0 ± 1.6	20.0 ± 2.2	9.0 ± 2.0
887	0.3 ± 0.4	0.4 ± 0.3	7065 ± 9	25	5	25.2 ± 1.4	12.6 ± 2.9	9.7 ± 2.1	16.7 ± 4.4	17.6 ± 2.5
889	-1.2 ± 0.4	-0.9 ± 0.4	4852 ± 7	20	10	64.4 ± 0.7	73.4 ± 3.9	9.9 ± 2.1	58.6 ± 2.9	14.8 ± 3.1
890	0.4 ± 0.5	-0.1 ± 0.4	6541 ± 10	15	–	142.6 ± 0.5	157.5 ± 4.2	11.0 ± 2.6	162.8 ± 5.4	14.1 ± 2.8
896	0.3 ± 0.5	1.7 ± 0.6	7439 ± 11	18	–	19.6 ± 0.5	18.7 ± 6.9	20.0 ± 5.5	29.6 ± 5.6	23.0 ± 4.6
904	-0.5 ± 0.5	-0.0 ± 0.5	4913 ± 13	30	6	148.2 ± 1.1	149.8 ± 2.5	14.2 ± 2.6	145.1 ± 2.6	12.7 ± 2.6
924	-1.0 ± 0.0	-1.0 ± 0.0	2571 ± 1	22	7	24.6 ± 0.8	37.4 ± 1.8	12.0 ± 1.7	51.4 ± 3.2	14.7 ± 3.7
929	1.4 ± 0.8	0.1 ± 0.7	7977 ± 17	20	–	43.4 ± 0.8	54.9 ± 4.6	16.8 ± 3.6	58.2 ± 4.0	15.5 ± 3.6
938	1.0 ± 0.6	1.7 ± 0.5	5896 ± 4	15	7	51.1 ± 5.9	75.3 ± 10.7	34.0 ± 6.3	73.2 ± 8.1	26.1 ± 5.4

Table B.3. Ionized gas kinematic properties of the non-interacting sample selected for this study included in the CALIFA survey.

id	$\Delta\alpha$	$\Delta\delta$	V_{sys}	r_{max}	r_{min}	PA_{morph} (r_{max})	PA approaching		PA receding	
							PA_{kin}	δPA_{kin}	PA_{kin}	δPA_{kin}
	(arcsec)	(arcsec)	(km s^{-1})	(arcsec)	(arcsec)	(°)	(°)	(°)	(°)	(°)
(1)	(2)	(3)	(4)	(5)	(6)	(7)	(8)	(9)	(10)	(11)
1	...	...	4990 ± 2	22	...	3.7 ± 0.4	4.5 ± 1.2	3.1 ± 1.0	3.5 ± 1.6	3.5 ± 1.3
2	0.2 ± 0.1	-2.3 ± 0.1	7247 ± 1	22	...	45.2 ± 0.9	55.0 ± 1.4	6.1 ± 0.7	44.6 ± 1.0	6.5 ± 1.5
7	-1.4 ± 0.3	-0.5 ± 0.4	6299 ± 18	20	...	17.4 ± 0.2	27.8 ± 2.7	8.6 ± 2.1	10.3 ± 2.4	6.8 ± 1.7
8	0.1 ± 0.1	0.9 ± 0.1	4534 ± 0	20	7	106.0 ± 1.1	116.2 ± 2.1	7.4 ± 1.0	115.7 ± 1.7	7.3 ± 1.0
10	0.1 ± 0.2	-0.7 ± 0.3	5974 ± 8	25	10	179.3 ± 0.6	16.4 ± 1.4	8.3 ± 1.5	18.9 ± 2.3	13.9 ± 2.5
23	-0.5 ± 0.6	-0.9 ± 0.6	3859 ± 6	20	10	126.0 ± 0.7	69.9 ± 16.1	91.4 ± 9.2	108.2 ± 33.0	91.4 ± 21.9
25	-1.8 ± 0.5	-1.2 ± 0.6	5239 ± 10	30	7	167.1 ± 1.0	174.6 ± 2.4	14.5 ± 3.2	165.6 ± 1.8	19.8 ± 2.7
28	-0.4 ± 0.2	0.0 ± 0.3	4486 ± 4	12	5	60.4 ± 0.8	56.2 ± 2.3	11.0 ± 2.6	47.3 ± 2.4	8.6 ± 2.5
30	0.1 ± 0.1	1.4 ± 0.1	4111 ± 2	20	7	177.3 ± 0.8	5.7 ± 1.9	6.8 ± 1.7	179.6 ± 0.6	6.9 ± 3.0
31	-0.8 ± 0.2	1.5 ± 0.2	4438 ± 2	30	5	82.2 ± 4.9	65.4 ± 1.1	7.2 ± 1.3	75.9 ± 1.9	10.5 ± 2.2
33	-0.2 ± 0.2	0.5 ± 0.2	5213 ± 6	20	7	93.7 ± 1.5	91.5 ± 2.1	7.5 ± 1.1	87.7 ± 1.2	6.9 ± 1.3
41	...	...	5547 ± 0	15	...	53.9 ± 0.2	45.9 ± 2.2	9.6 ± 2.4	60.6 ± 2.2	6.1 ± 1.3
43	-0.1 ± 0.3	1.0 ± 0.4	4811 ± 7	12	7	156.4 ± 1.0	7.9 ± 4.0	12.3 ± 3.8	16.1 ± 4.5	11.5 ± 4.3
53	-1.2 ± 0.3	-1.8 ± 0.3	6356 ± 4	20	...	152.2 ± 0.5	148.0 ± 1.4	4.8 ± 1.0	151.7 ± 1.6	5.8 ± 1.2
108	0.1 ± 0.2	-0.1 ± 0.3	5235 ± 2	20	5	96.5 ± 1.2	100.6 ± 2.2	8.5 ± 2.0	100.4 ± 2.3	9.0 ± 2.4
116	-0.7 ± 0.4	1.4 ± 0.4	7696 ± 12	10	...	172.4 ± 1.4	159.9 ± 4.9	8.3 ± 2.7	167.3 ± 7.0	12.3 ± 5.0
131	-0.1 ± 0.5	-0.4 ± 0.5	3693 ± 7	18	...	128.0 ± 0.4	130.3 ± 3.5	8.2 ± 2.5	132.9 ± 2.9	7.0 ± 1.9
147	0.1 ± 0.1	2.2 ± 0.2	3568 ± 2	25	7	141.7 ± 1.9	117.7 ± 1.4	8.1 ± 1.4	116.4 ± 4.3	14.3 ± 2.6
149	0.6 ± 0.2	-0.6 ± 0.2	4359 ± 10	20	5	3.9 ± 0.8	5.3 ± 1.7	4.7 ± 0.9	13.8 ± 1.7	5.9 ± 1.5
151	0.7 ± 0.3	-0.3 ± 0.2	4574 ± 18	29	...	37.0 ± 0.3	36.6 ± 1.3	4.3 ± 0.8	37.3 ± 3.0	10.8 ± 3.7
152	-0.1 ± 0.3	-1.1 ± 0.3	3916 ± 4	20	...	121.9 ± 0.5	122.8 ± 1.9	8.2 ± 2.2	113.9 ± 2.2	8.1 ± 1.8
153	-0.6 ± 0.4	-0.7 ± 0.3	8081 ± 10	20	...	134.9 ± 0.3	135.7 ± 2.1	7.3 ± 1.8	134.0 ± 1.9	4.8 ± 1.1
273	2.4 ± 0.9	-1.9 ± 0.6	4270 ± 5	33	...	162.9 ± 0.2	150.0 ± 2.9	10.7 ± 2.1	174.1 ± 2.6	6.2 ± 1.5
275	1.2 ± 0.2	0.6 ± 0.1	2086 ± 6	27	5	82.1 ± 0.6	83.2 ± 0.9	3.9 ± 0.8	82.3 ± 1.3	8.1 ± 1.9
277	0.9 ± 0.4	0.4 ± 0.6	3649 ± 6	25	9	22.3 ± 0.7	12.8 ± 2.5	16.1 ± 2.8	32.5 ± 4.0	26.6 ± 3.1
307	-0.2 ± 0.3	0.2 ± 0.3	8439 ± 10	15	...	95.2 ± 0.5	97.2 ± 4.3	9.1 ± 3.4	92.0 ± 3.2	6.3 ± 2.5
364	0.2 ± 0.6	1.1 ± 0.6	6582 ± 22	25	...	99.8 ± 0.4	108.6 ± 4.3	14.3 ± 2.7	98.6 ± 2.8	6.4 ± 1.7
386	-0.7 ± 0.5	-0.1 ± 0.6	6332 ± 10	17	...	48.9 ± 0.9	46.6 ± 3.4	8.8 ± 2.6	44.2 ± 2.9	10.6 ± 2.6
414	-0.4 ± 0.3	0.1 ± 0.3	2497 ± 3	25	7	107.9 ± 3.2	143.4 ± 2.3	13.8 ± 2.6	150.5 ± 2.8	17.1 ± 3.7
436	0.1 ± 0.3	-1.5 ± 0.3	3158 ± 6	20	5	24.3 ± 1.1	171.5 ± 3.1	12.1 ± 4.7	173.7 ± 2.7	7.7 ± 1.9
489	0.8 ± 0.1	-0.6 ± 0.2	3409 ± 1	25	10	104.1 ± 1.0	100.8 ± 1.5	8.8 ± 1.3	104.2 ± 2.0	8.1 ± 1.2
515	0.1 ± 0.4	0.1 ± 0.3	3866 ± 7	25	10	0.2 ± 1.1	166.6 ± 3.3	10.5 ± 1.9	165.4 ± 3.2	10.1 ± 1.8
518	-0.6 ± 0.5	-0.5 ± 0.2	2690 ± 11	30	5	88.5 ± 1.0	98.1 ± 2.9	13.7 ± 1.9	97.3 ± 2.5	14.2 ± 3.1
580	0.0 ± 0.2	-0.0 ± 0.2	4063 ± 2	23	5	43.3 ± 0.5	40.1 ± 1.5	6.6 ± 1.6	35.5 ± 1.6	7.8 ± 1.2
602	...	...	4799 ± 12	15	...	75.2 ± 0.8	67.0 ± 3.7	23.9 ± 6.9	59.3 ± 6.5	19.8 ± 4.8
610	0.5 ± 0.4	1.1 ± 0.5	7223 ± 12	20	...	39.4 ± 0.3	39.9 ± 2.0	5.6 ± 1.3	47.0 ± 2.6	7.1 ± 1.5
624	0.9 ± 0.6	-0.3 ± 0.4	7309 ± 7	25	6	116.4 ± 1.5	87.4 ± 4.6	25.9 ± 5.1	78.1 ± 7.9	38.4 ± 4.2
630	-0.1 ± 0.4	0.0 ± 0.5	1727 ± 7	20	9	146.4 ± 0.7	159.5 ± 4.0	18.5 ± 4.4	163.9 ± 3.7	18.1 ± 4.3
664	...	...	3204 ± 5	25	...	118.7 ± 0.2	113.3 ± 3.2	19.8 ± 3.3	103.6 ± 3.2	13.6 ± 3.5
684	0.4 ± 0.4	1.2 ± 0.4	5439 ± 10	27	7	141.2 ± 2.1	109.5 ± 3.8	15.3 ± 4.5	111.3 ± 4.2	15.0 ± 2.0
714	-0.2 ± 0.2	0.4 ± 0.2	7831 ± 10	20	...	16.7 ± 0.5	12.1 ± 2.4	5.6 ± 1.3	13.5 ± 1.9	4.3 ± 1.0
715	-1.0 ± 0.1	0.7 ± 0.0	1884 ± 1	30	7	66.5 ± 0.4	64.9 ± 0.5	4.3 ± 0.6	66.7 ± 0.8	7.3 ± 1.6
743	0.3 ± 0.2	-0.3 ± 0.1	3865 ± 5	25	5	85.9 ± 0.5	83.0 ± 1.6	6.0 ± 0.9	84.9 ± 1.3	8.5 ± 1.0
748	-0.9 ± 0.1	-2.7 ± 0.1	2350 ± 2	25	10	192.5 ± 0.5	10.7 ± 0.7	6.1 ± 1.0	21.4 ± 1.4	10.3 ± 1.4
753	0.8 ± 0.1	-0.6 ± 0.1	3222 ± 4	25	7	56.1 ± 0.6	58.4 ± 0.7	8.4 ± 0.7	55.7 ± 0.6	4.0 ± 0.4
764	-0.9 ± 0.3	0.7 ± 0.2	7726 ± 12	20	7	128.4 ± 0.7	129.4 ± 2.8	10.2 ± 2.4	128.4 ± 2.3	12.4 ± 3.9
768	0.4 ± 0.2	-0.0 ± 0.2	3765 ± 3	15	7	42.4 ± 0.9	36.8 ± 1.5	8.5 ± 1.8	53.7 ± 1.8	7.7 ± 1.8
771	2.2 ± 0.3	-0.5 ± 0.4	3741 ± 9	20	7	98.7 ± 0.9	40.7 ± 3.9	15.8 ± 2.7	44.3 ± 2.8	11.5 ± 2.9
777	-0.5 ± 0.2	0.6 ± 0.2	4877 ± 9	30	10	36.1 ± 0.4	37.4 ± 1.0	4.7 ± 0.9	36.4 ± 1.2	6.0 ± 1.0
779	-0.1 ± 0.3	-1.1 ± 0.3	5559 ± 5	23	...	121.8 ± 0.3	124.9 ± 2.1	6.5 ± 1.3	122.5 ± 2.0	8.4 ± 1.7
782	0.3 ± 0.5	0.5 ± 0.5	7878 ± 29	12	...	152.9 ± 0.5	153.0 ± 3.6	10.4 ± 2.9	149.0 ± 4.6	11.9 ± 3.1

Notes. (1) CALIFA identifier. (2) and (3) Location of the kinematic centre. The value listed is the gradient peak (GP) with respect to the optical nucleus (ON) if not, ON is used as kinematic centre (see section 3 for details). (4) systemic velocity derived from integrated the velocities in a 2.7″ aperture centred in the kinematic centre. (5) radius used to average the polar coordinates of the positions from the lines of nodes (see section 3 for details). (6) radius used to average the polar coordinates of the positions from the cero-velocity line (see section 3 for details). (7) morphological PA inferred by fitting an elipse to an isophote at radius r_{max} in the r-band SDSS image. (8) kinematic position angle at radius r for the approaching side (see section 3 for details). (9) standard deviation of the kinematic position angle of the approaching side (see section 3 for details). (10) kinematic position angle at radius r for the receding side. (11) standard deviation of the kinematic position angle of the receding side. Values in parenthesis for each row represent the errors obtained from Monte Carlo simulations.

Table B.3. continue B.3

id	$\Delta\alpha$	$\Delta\delta$	V_{sys}	r_{max}	r_{min}	PA_{morph} (r_{max})	PA approaching		PA receding	
							PA_{kin}	δPA_{kin}	PA_{kin}	δPA_{kin}
	(arcsec)	(arcsec)	(km s^{-1})	(arcsec)	(arcsec)	(°)	(°)	(°)	(°)	(°)
(1)	(2)	(3)	(4)	(5)	(6)	(7)	(8)	(9)	(10)	(11)
790	1.8 ± 0.3	0.9 ± 0.3	4717 ± 6	12	5	143.6 ± 1.3	145.5 ± 3.7	11.1 ± 1.9	160.7 ± 5.9	12.7 ± 3.3
791	-0.5 ± 0.2	-0.3 ± 0.2	3276 ± 4	30	...	152.3 ± 0.3	154.1 ± 1.1	3.8 ± 0.7	148.9 ± 1.0	3.2 ± 0.4
804	-3.1 ± 0.4	-2.4 ± 0.5	3486 ± 7	15	...	126.8 ± 0.5	124.7 ± 4.7	25.2 ± 6.7	109.5 ± 15.9	71.6 ± 12.6
810	0.7 ± 0.1	1.1 ± 0.1	4093 ± 1	25	...	15.3 ± 0.5	15.4 ± 0.7	4.1 ± 0.8	15.1 ± 0.6	5.7 ± 0.8
813	-0.6 ± 0.1	0.0 ± 0.2	3818 ± 1	28	7	113.1 ± 8.8	101.9 ± 2.0	15.8 ± 2.7	90.5 ± 3.0	13.8 ± 3.8
823	-1.0 ± 0.2	1.9 ± 0.3	2825 ± 2	25	7	159.2 ± 0.6	149.6 ± 2.1	8.3 ± 1.4	158.6 ± 2.1	10.7 ± 2.0
824	-0.4 ± 0.1	-0.6 ± 0.2	4732 ± 3	27	...	159.8 ± 0.2	159.3 ± 1.0	5.4 ± 1.2	161.7 ± 1.2	5.5 ± 1.1
826	...	...	5014 ± 2	25	...	127.9 ± 0.3	123.9 ± 1.8	12.4 ± 2.2	129.9 ± 2.2	17.9 ± 3.3
831	0.2 ± 0.1	0.5 ± 0.2	4968 ± 4	15	...	123.4 ± 0.6	124.2 ± 1.5	6.6 ± 1.2	127.1 ± 1.2	5.3 ± 0.9
834	-0.4 ± 0.5	1.3 ± 0.5	8764 ± 14	15	...	114.2 ± 0.5	101.9 ± 3.7	11.8 ± 4.3	106.8 ± 3.7	7.5 ± 2.1
836	1.1 ± 0.2	1.9 ± 0.2	2407 ± 0	29	...	148.9 ± 0.9	120.9 ± 1.7	10.9 ± 1.9	135.6 ± 2.2	17.5 ± 2.6
842	0.0 ± 0.3	-0.2 ± 0.3	2955 ± 6	30	7	54.7 ± 0.4	56.8 ± 2.4	9.6 ± 1.5	63.2 ± 2.6	15.6 ± 1.8
853	0.8 ± 0.2	-1.0 ± 0.2	3809 ± 3	30	10	53.0 ± 5.0	50.3 ± 0.9	2.9 ± 0.3	47.3 ± 1.2	3.3 ± 0.4
854	0.9 ± 0.4	0.2 ± 0.2	8654 ± 16	20	...	90.9 ± 0.4	87.4 ± 2.3	10.1 ± 2.8	86.2 ± 3.1	9.7 ± 2.9
856	0.7 ± 0.1	2.1 ± 0.2	4700 ± 3	22	5	91.6 ± 0.7	94.3 ± 2.6	10.4 ± 2.5	91.8 ± 2.6	6.9 ± 1.8
857	-2.0 ± 0.6	-1.5 ± 0.4	8539 ± 8	15	...	36.1 ± 0.4	60.5 ± 3.7	12.6 ± 5.6	38.2 ± 4.3	11.7 ± 3.1
862	-1.3 ± 0.2	1.0 ± 0.2	6720 ± 4	25	...	32.1 ± 0.4	27.8 ± 1.2	4.9 ± 1.0	37.8 ± 1.7	7.3 ± 0.7
869	1.3 ± 0.6	3.0 ± 0.4	6139 ± 18	22	7	121.8 ± 1.8	125.9 ± 3.0	13.4 ± 3.7	133.0 ± 2.7	12.3 ± 2.5
872	2.0 ± 0.7	1.1 ± 0.6	3813 ± 22	20	7	85.4 ± 3.0	64.3 ± 5.3	36.8 ± 3.2	45.3 ± 6.7	30.3 ± 5.8
876	0.1 ± 0.3	-1.2 ± 0.2	5743 ± 4	20	5	106.9 ± 1.3	98.1 ± 2.4	8.8 ± 1.7	96.7 ± 3.2	14.2 ± 3.8
886	-0.3 ± 0.1	0.1 ± 0.2	4455 ± 5	27	7	12.8 ± 0.3	10.3 ± 1.2	6.0 ± 1.4	17.2 ± 1.1	7.0 ± 1.2
887	0.8 ± 0.1	0.9 ± 0.1	7056 ± 3	25	5	25.2 ± 1.4	15.3 ± 1.8	8.6 ± 1.2	15.0 ± 1.6	7.3 ± 1.5
889	-0.5 ± 0.0	0.5 ± 0.1	4883 ± 0	20	10	64.4 ± 0.7	61.7 ± 1.2	6.3 ± 0.9	70.7 ± 1.2	5.4 ± 1.2
890	2.1 ± 0.4	-1.2 ± 0.4	6533 ± 5	15	...	142.6 ± 0.5	144.5 ± 3.0	13.9 ± 4.0	167.8 ± 4.2	9.7 ± 3.8
896	0.9 ± 0.2	0.0 ± 0.3	7461 ± 6	18	...	19.6 ± 0.5	18.2 ± 2.7	7.7 ± 1.4	28.1 ± 1.8	6.8 ± 1.7
904	-0.6 ± 0.1	1.5 ± 0.1	4892 ± 0	30	6	148.2 ± 1.1	145.1 ± 1.5	8.4 ± 1.1	147.2 ± 0.7	5.9 ± 1.1
924	-0.2 ± 0.4	-0.3 ± 0.4	2525 ± 12	22	7	24.6 ± 0.8	49.3 ± 3.9	13.4 ± 2.9	52.0 ± 2.7	13.8 ± 3.7
929	-2.0 ± 0.3	1.4 ± 0.3	8103 ± 6	20	...	43.4 ± 0.8	52.4 ± 1.3	7.1 ± 1.5	50.7 ± 1.9	7.6 ± 1.8
938	0.6 ± 0.2	0.7 ± 0.2	5913 ± 3	15	7	51.1 ± 5.9	64.6 ± 3.9	14.6 ± 3.4	68.4 ± 5.2	12.3 ± 3.4

Table B.4. Kinematic orientation measured at different radius for a sample of low inclined galaxies included in our sample of non-interacting galaxies.

id					Stars				Ionized gas			
					r_{in}		r_{out}		r_{in}		r_{out}	
	r_{in}^{stars}	r_{out}^{stars}	r_{in}^{gas}	r_{out}^{gas}	PA_{app}	PA_{rec}	PA_{app}	PA_{rec}	PA_{app}	PA_{rec}	PA_{app}	PA_{rec}
	(arcsec)	(arcsec)	(arcsec)	(arcsec)	(degrees)	(degrees)	(degrees)	(degrees)	(degrees)	(degrees)	(degrees)	(degrees)
(1)	(2)	(3)	(4)	(5)	(6)	(7)	(8)	(9)	(10)	(11)	(12)	(13)
8	10	20	14	28	114	117	114	112	114	114	114	117
10	12	25	12	27	27	15	12	12	18	13	15	17
23	15	25	27	30	81	84	103	89	77	102	76	76
25	22	30	22	30	170	166	155	171	170	166	168	155
28	14	17	14	28	52	42	72	52	55	48	49	51
30	7	20	7	30	183	162	189	168	12	162	6	91
31	15	30	16	32	57	74	72	64	67	72	65	73
33	10	20	16	32	93	90	88	95	91	86	90	95
43	8	17	8	17	22	29	9	20	7	19	99	10
108	10	20	10	27	86	90	96	107	94	95	100	97
147	10	20	10	30	117	116	112	125	117	115	117	115
149	12	25	12	28	10	10	6	4	5	18	5	12
275	13	27	16	32	78	76	79	94	83	80	82	86
277	12	25	16	30	15	20	23	13	49	46	12	21
414	14	25	14	30	137	136	147	144	133	137	146	152
436	14	25	23	25	164	181	178	175	172	173	178	178
489	13	27	16	32	102	110	95	102	98	106	105	99
515	15	25	16	32	162	168	163	172	164	162	166	169
518	17	30	17	30	105	93	90	98	104	97	95	98
580	11	23	13	27	35	37	47	33	35	31	42	35
602	11	22	5	10	68	81	75	84	71	80	65	63
624	21	25	21	30	90	82	105	100	74	70	92	89
630	12	22	12	32	160	97	155	158	167	163	159	157
684	15	27	20	30	119	111	121	105	114	114	107	108
715	15	30	16	32	72	59	66	61	65	67	64	58
743	12	25	16	32	80	84	94	78	81	84	81	83
748	12	25	16	30	12	20	18	19	12	24	13	22
753	12	25	16	32	54	57	55	54	53	57	62	56
764	7	20	7	30	132	124	119	138	120	113	130	128
768	7	15	14	28	38	25	42	42	35	53	38	47
771	10	20	21	30	21	33	35	38	39	41	48	33
777	15	30	18	35	36	38	32	38	38	34	36	34
790	6	12	10	20	137	143	144	146	144	162	149	155
791	15	30	15	30	151	154	149	154	156	149	153	149
813	16	28	16	35	106	88	93	88	101	83	99	95
823	12	25	16	32	156	165	160	161	149	162	152	154
836	14	29	14	29	144	135	131	129	127	138	119	129
842	18	30	15	30	90	73	57	60	58	70	55	52
853	15	30	15	30	53	46	56	50	49	45	50	48
856	7	22	7	30	84	98	95	89	76	88	94	93
869	16	22	16	30	130	142	116	132	134	136	124	133
872	17	20	17	30	63	55	75	65	61	39	73	71
876	10	20	15	25	94	79	96	110	102	89	92	101
886	13	27	16	32	2	24	4	18	15	16	7	15
887	10	25	10	35	10	10	15	24	11	15	14	13
889	11	22	11	28	71	58	74	58	57	66	63	69
904	11	30	11	30	143	138	152	146	142	143	145	148
924	11	22	16	32	39	48	33	51	43	53	46	48
938	11	20	11	30	78	72	67	74	64	69	66	66

Notes. (1) CALIFA identifier. (2) and (3) internal and external radii used to measured the kinematic PA in the stellar component (see section 4.3 for details). (4) and (5) internal and external radii used to measured the kinematic PA in the ionized gas component. (6) and (7) internal approaching and receding kinematic position angles for the stellar component (see section 4.3 for details). (8) and (9) external approaching and receding kinematic position angles for the stellar component. (10) and (11) internal approaching and receding kinematic position angles for the ionized gas. (12) and (13) external approaching and receding kinematic position angles for the ionized gas.

Appendix C: Stellar and Ionized velocity fields

In this appendix we present the velocity field of the 80 non-interacting galaxies. Each row present one galaxy similar as in Fig.1. From left to right: SDSS r-band image of the galaxy. White solid line represents the photometric PA measured at the same galactocentric distance as the kinematic PA (PA_{morph}, see section 3). Dashed line represents the photometric PA measured at the outermost isophote of the image (PA^{out}_{morph}, see section 4.3). Next two panels show the stellar and ionised gas velocity maps, respectively. Green points highlight the locations where the maximum velocity is located at given radius, determined from the position-velocity diagram. Black lines for each kinematic side represent the average kinematic PA (PA_{kin}), while white thin lines along the zero-velocity curve show the average minor kinematic PA. Next panel shows the distance from the galactic centre versus the maximum for the stellar (blue) and ionised gas (red) components. The curve along $0\,km\,s^{-1}$ represent the velocities along the zero-velocity curve. Uncertainty in velocity are determined from Monte Carlo simulations. Last panel shows the dependence of the different PA with respect to the radius. PA_{morph}, $PA^{stellar}_{kin}$ and PA^{gas}_{kin} are represented by open circles, filled blue diamonds and filled red squares, respectively. For barred galaxies we highlight with dashed lines the length of the bar and its orientation.

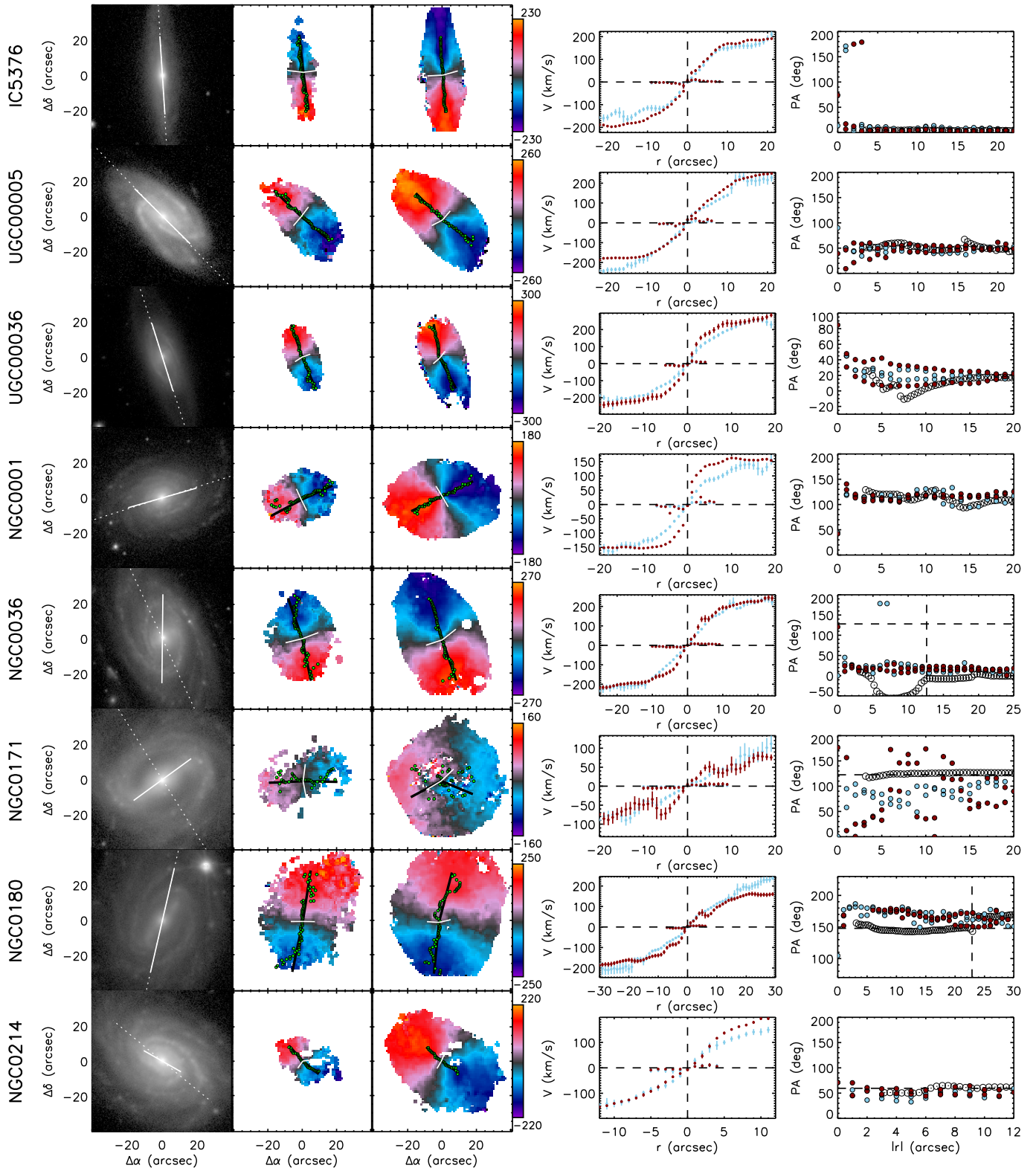

Fig. C.1. Stellar and ionised gas velocity fields for the sample of galaxies used in this study.

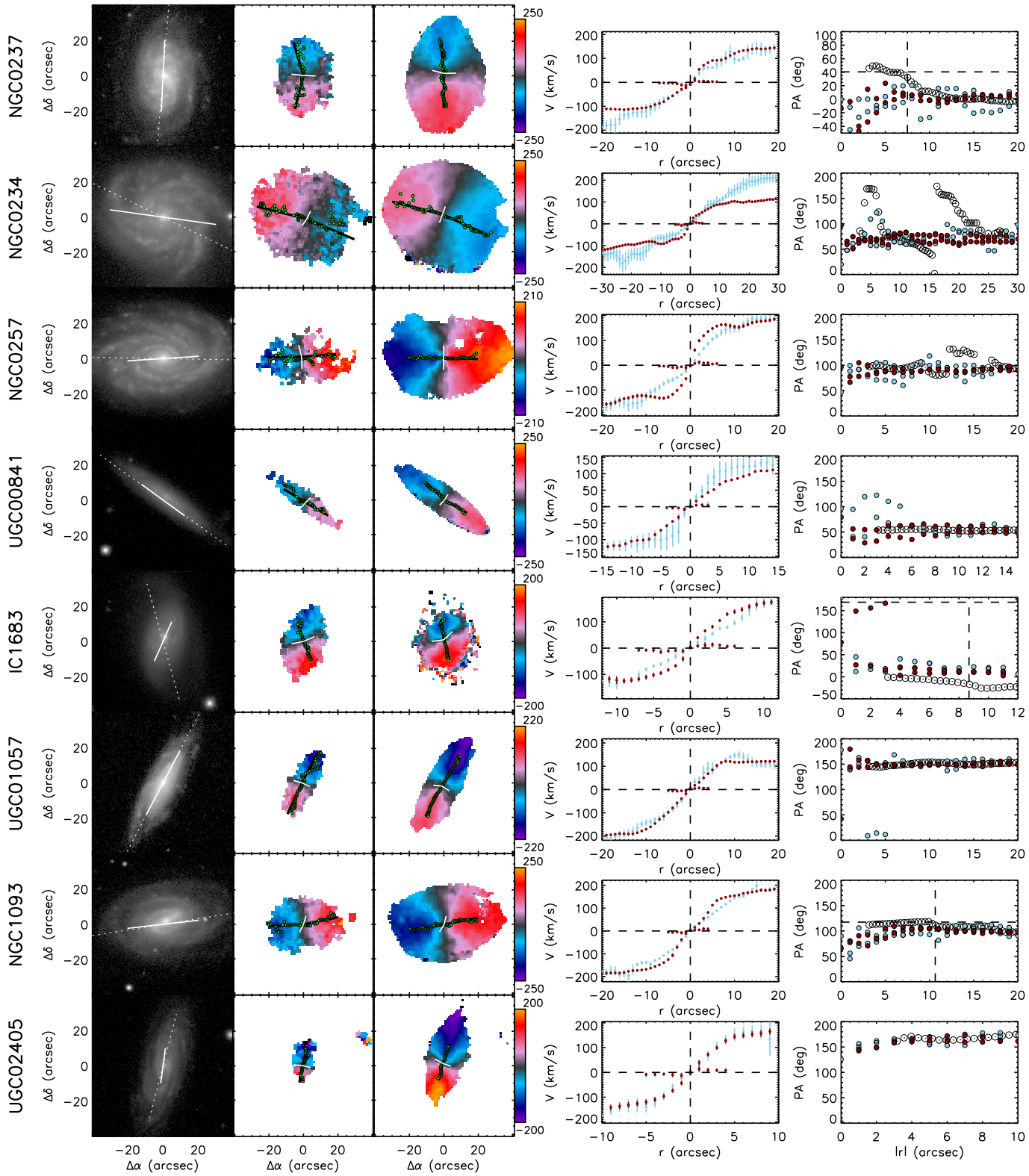

Fig. C.1. *- continued*

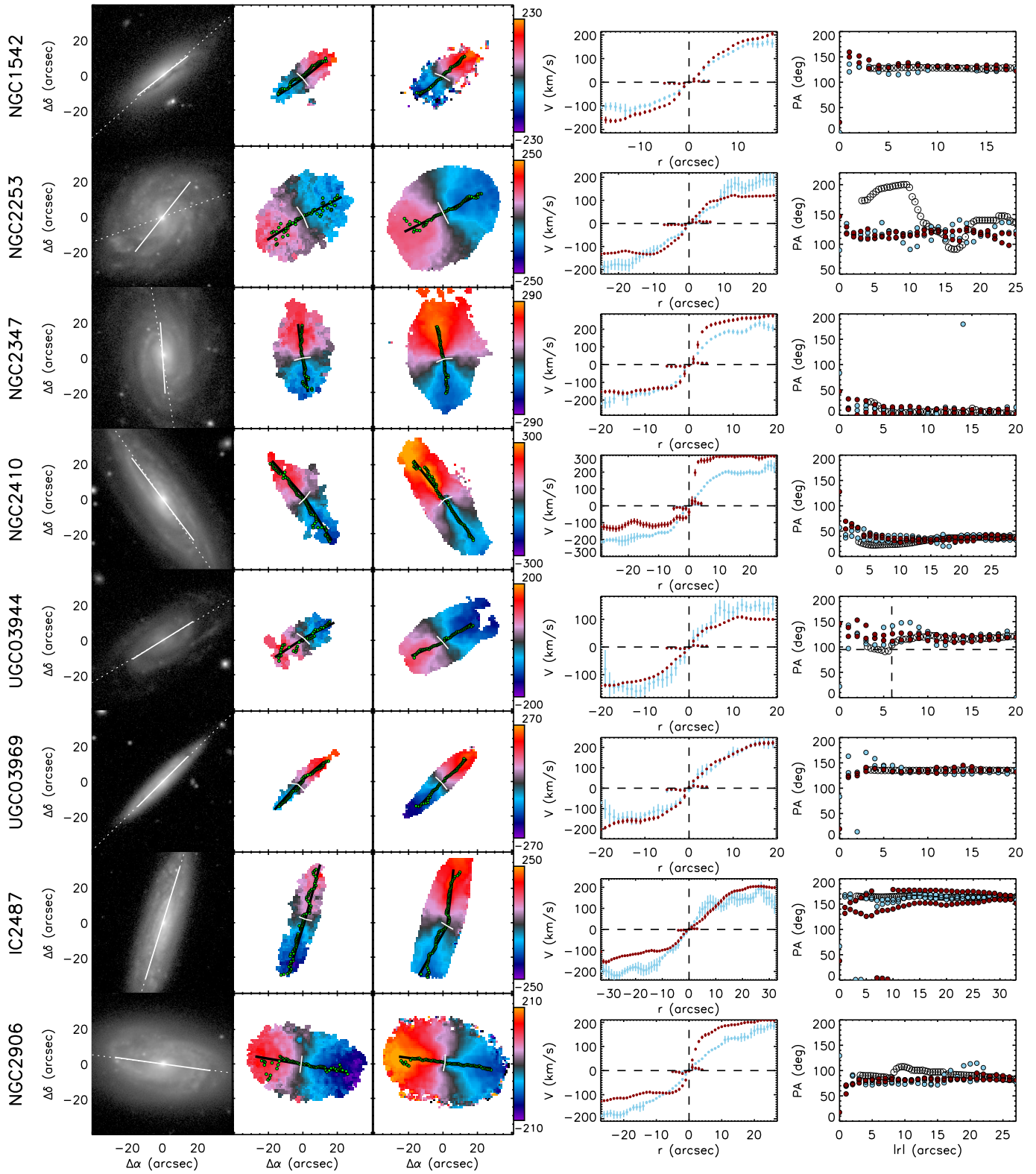

Fig. C.1. *- continued*

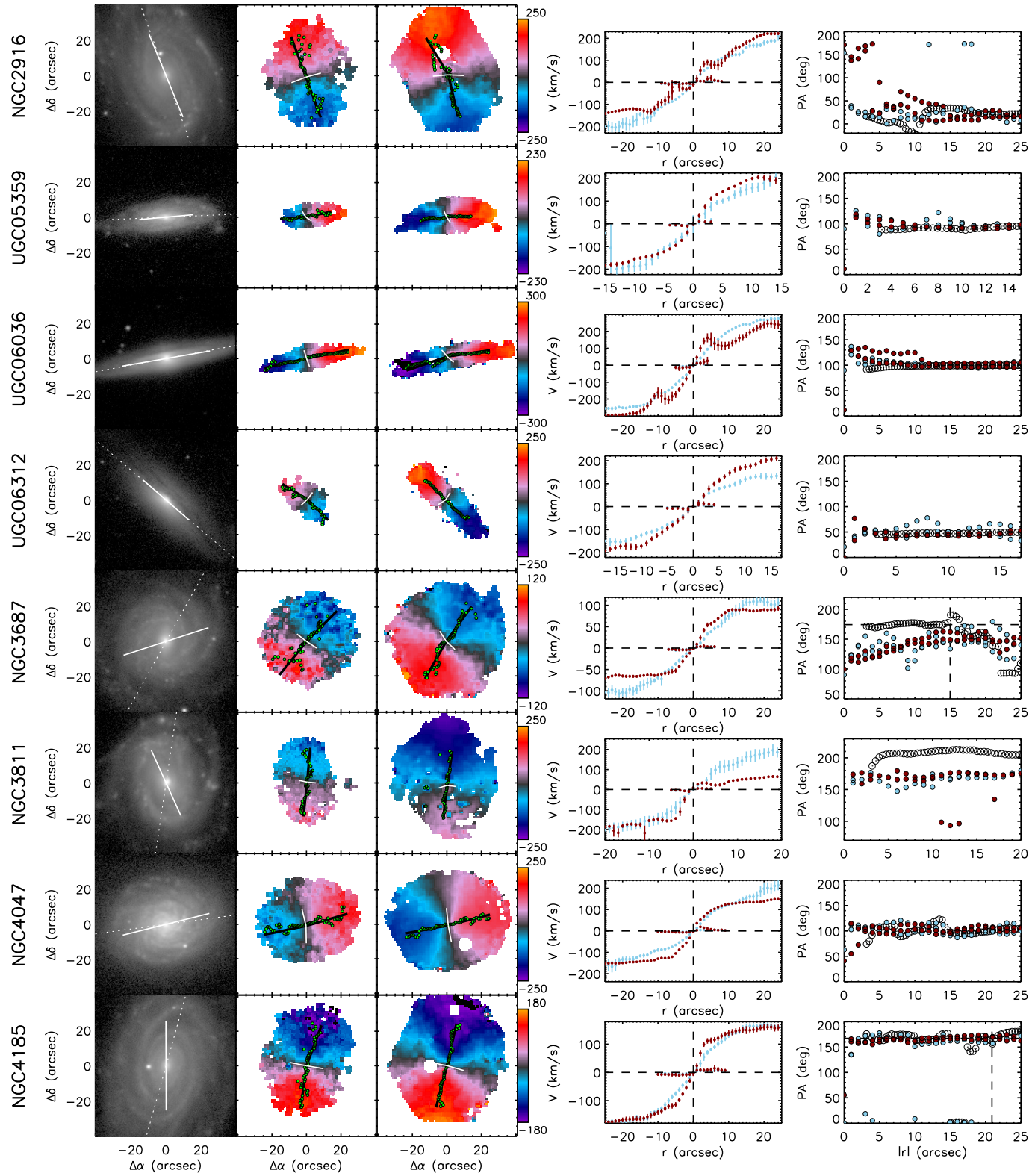

Fig. C.1. *- continued*

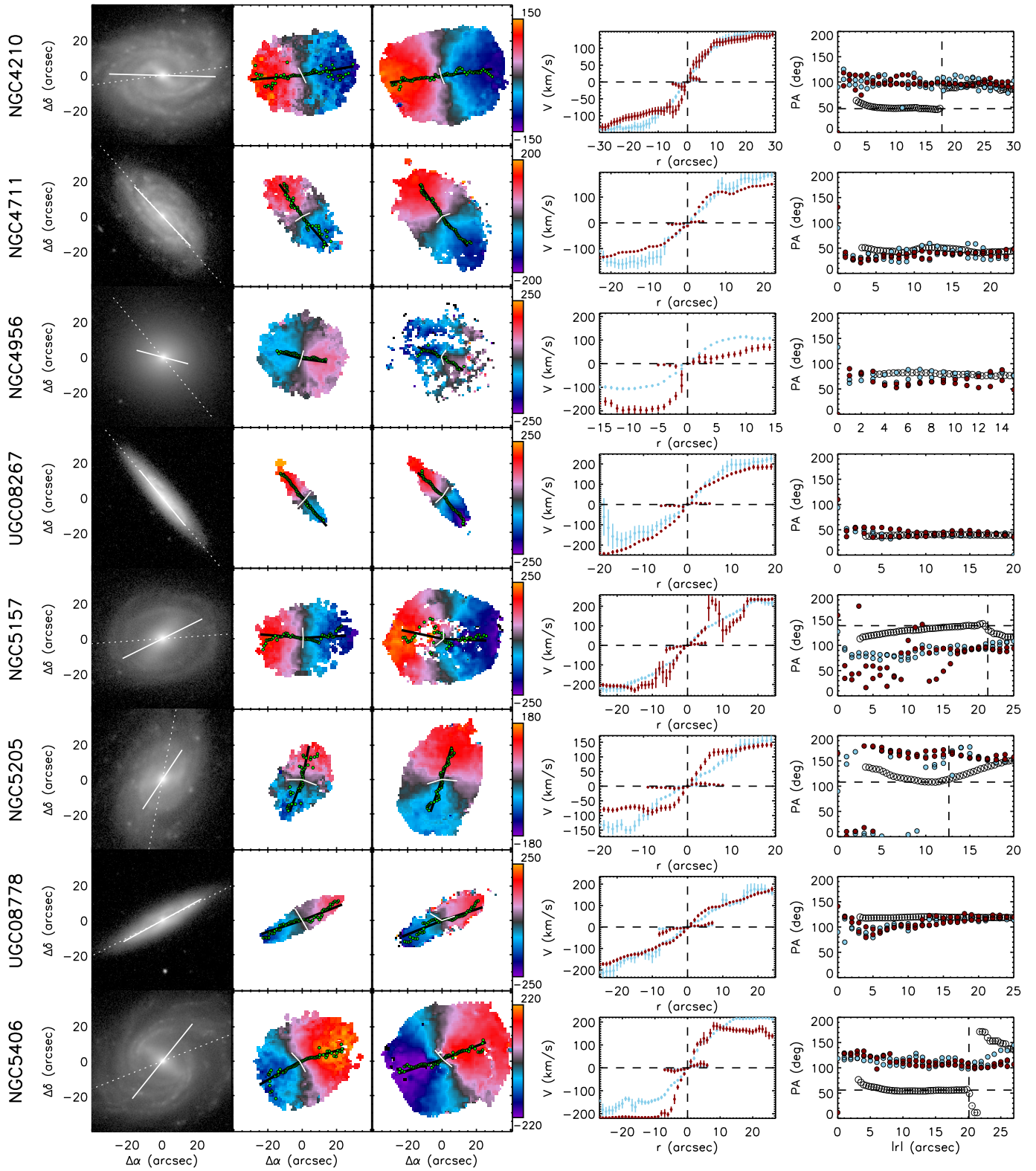

Fig. C.1. *- continued*

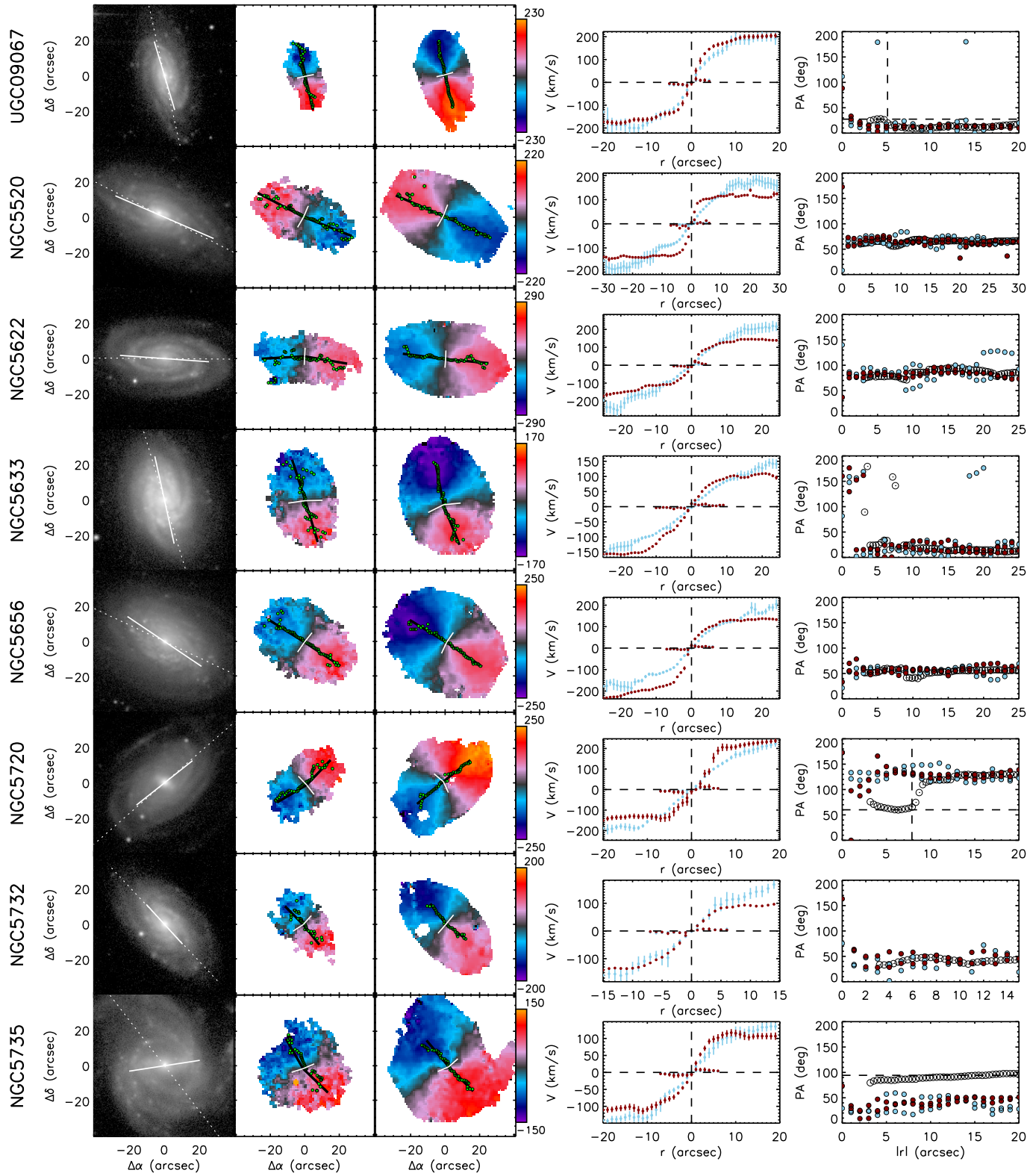

Fig. C.1. *- continued*

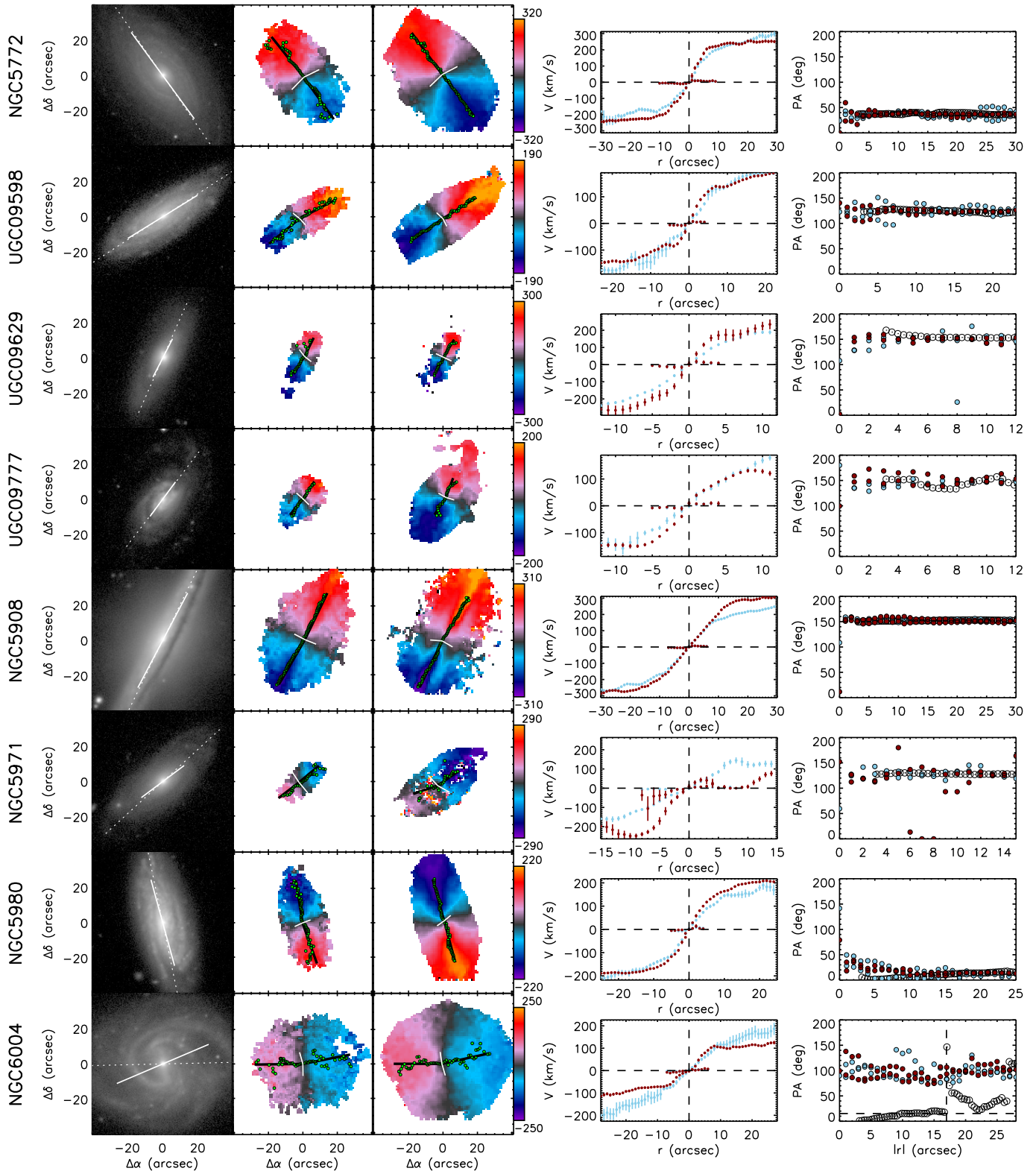

Fig. C.1. *- continued*

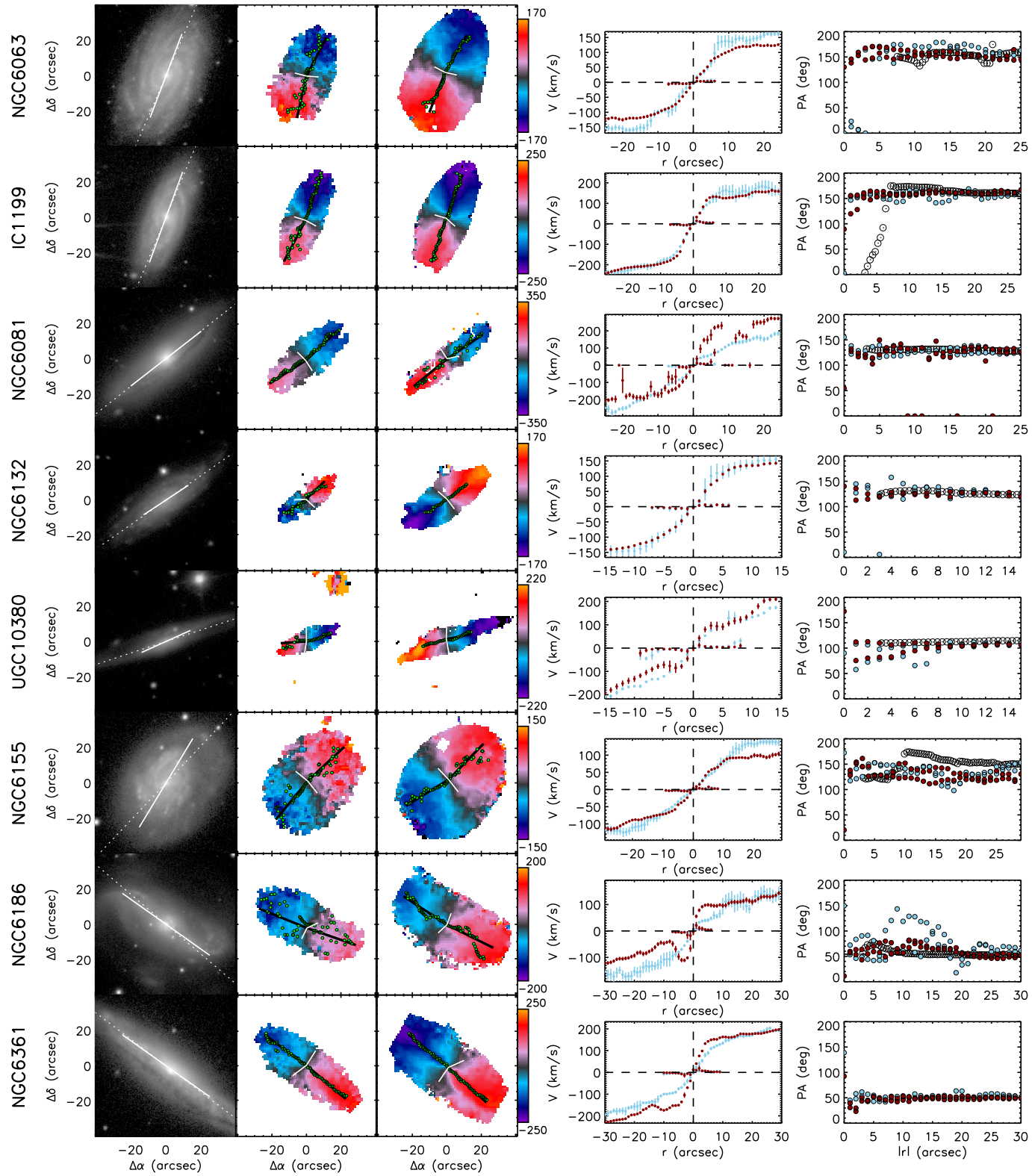

Fig. C.1. *- continued*

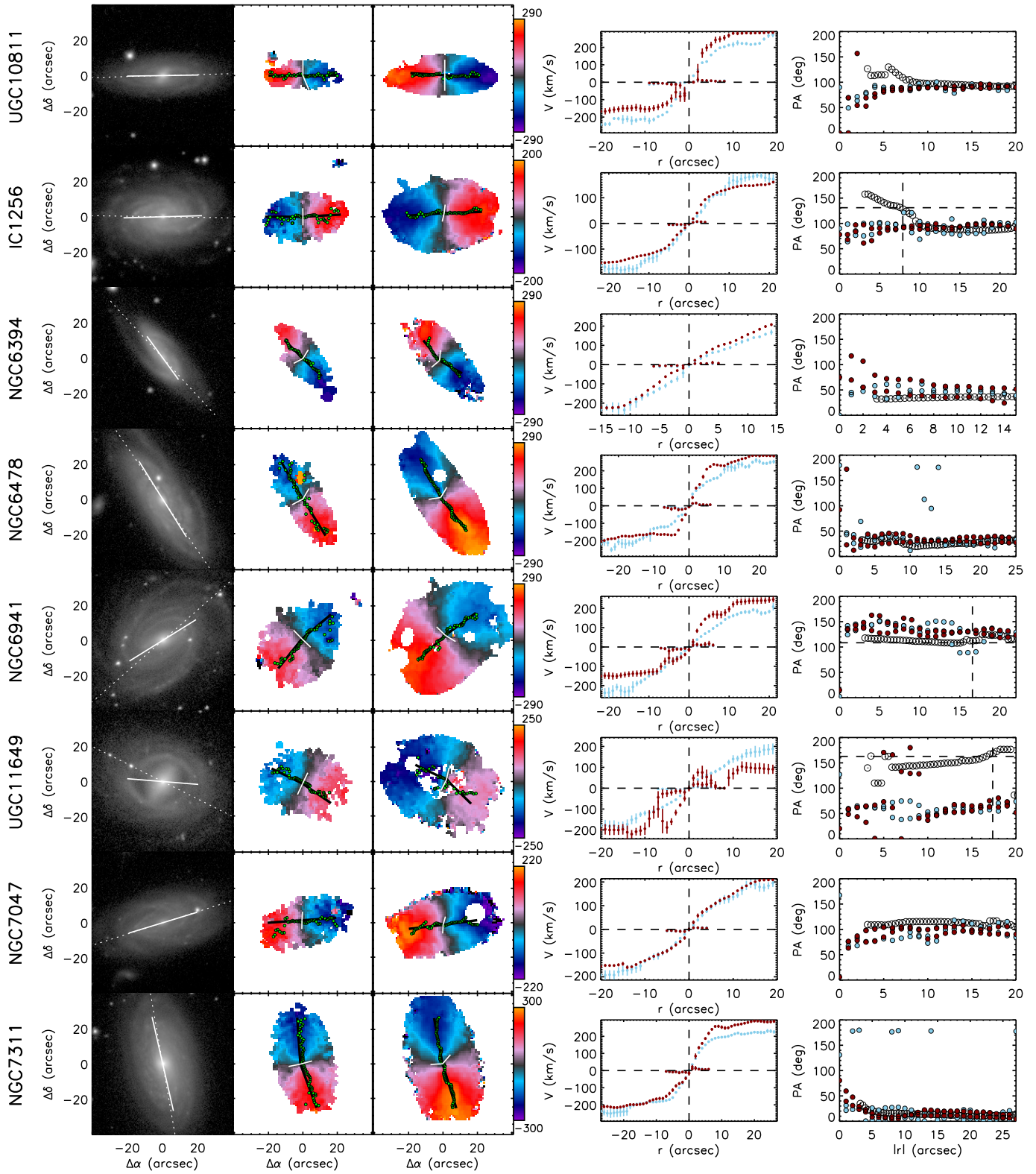

Fig. C.1. *- continued*

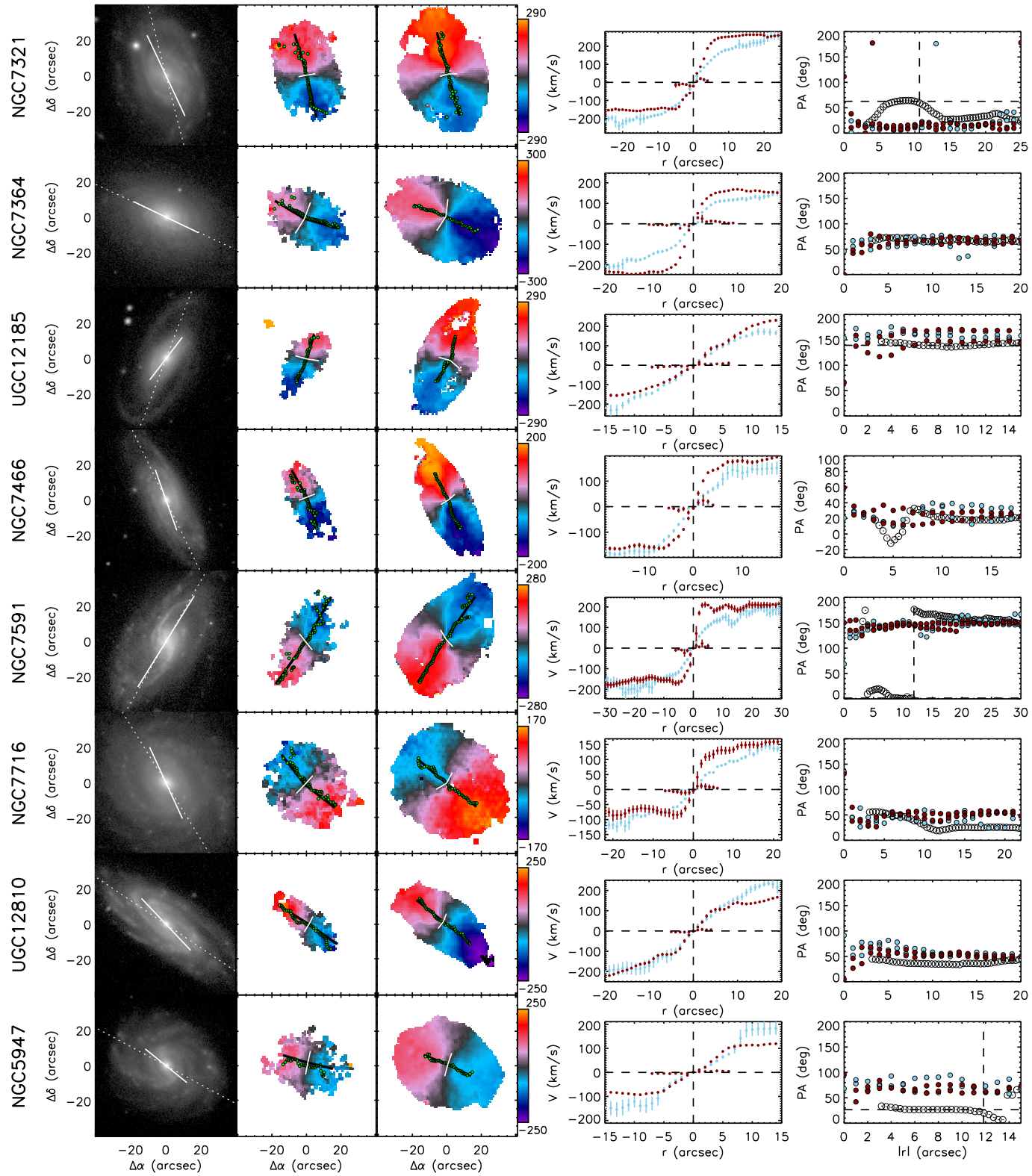

Fig. C.1. *- continued*